

Technische Universität München

FAKULTÄT FÜR PHYSIK
Dense and Strange Hadronic Matter

**First Measurement of the
 ϕ -Proton Correlation Function with
ALICE
in pp Collisions at $\sqrt{s}=13$ TeV**

Bachelorarbeit

von

Emma Chizzali

Aufgabensteller: Prof. Dr. Laura Fabbietti
Betreuer: M.Sc. Andreas Mathis
M.Sc. Bernhard Hohlweger
Abgabetermin: 11.09.2019

Contents

Abstract	iv
1 Introduction	1
2 Femtoscopy	5
2.1 The correlation function	5
2.1.1 Experimental Definition	6
2.1.2 Theoretical Definition	6
2.2 Lednicky Model	7
2.3 CATS	8
2.4 Corrections	8
3 Experimental Setup	10
3.1 The LHC	10
3.2 The ALICE Experiment	11
3.2.1 Inner Tracking System (ITS)	12
3.2.2 Time Projection Chamber (TPC)	12
3.2.3 Time Of Flight Chamber (TOF)	14
3.3 Track reconstruction	15
3.4 AliRoot	16
4 Data Analysis	17
4.1 Event selection	17
4.1.1 Event shape	19
4.2 Particle selection	21
4.2.1 Proton candidates	21
4.2.2 ϕ -meson candidates	22
5 Correlation function	27
5.1 Minimum Bias	27
5.2 High Multiplicity	29
5.2.1 Sphericity vs. spherocity	31
5.2.2 Background	32
5.2.3 Fit with CATS	35
6 Summary and Outlook	38

Abstract

In this work the interaction between protons and ϕ -mesons is studied for the first time. The ϕ -proton correlation function is measured with ALICE at the Large Hadron Collider (LHC) in pp collisions at $\sqrt{s}=13$ TeV. Both minimum bias (MB) and high multiplicity (HM) triggered data is investigated using the femtoscopy technique. The ϕ candidates are reconstructed via the channel $\phi \rightarrow K^+K^-$. A non-femtoscopic background in form of mini-jets, also known from previous meson-baryon analyses, is present and significantly reduced using event shape cuts. Due to the modest purity of the reconstructed ϕ candidates additional contributions from the combinatorial p-(K^+K^-) background have to be taken into account. The ϕ -proton interaction is found to be attractive and the correlation function obtained from HM data, which has sizably smaller uncertainties than the one from MB, is then fitted with CATS using the Lednicky model to determine the scattering parameters. From this an inverse scattering length of $1/f_0 = 1.9 \pm 0.7 \text{ fm}^{-1}$ and an effective range of $d_0 = 17 \pm 5 \text{ fm}$ is obtained. This demonstrates the feasibility of such analyses and could support future studies to determine the coupling constant.

1 Introduction

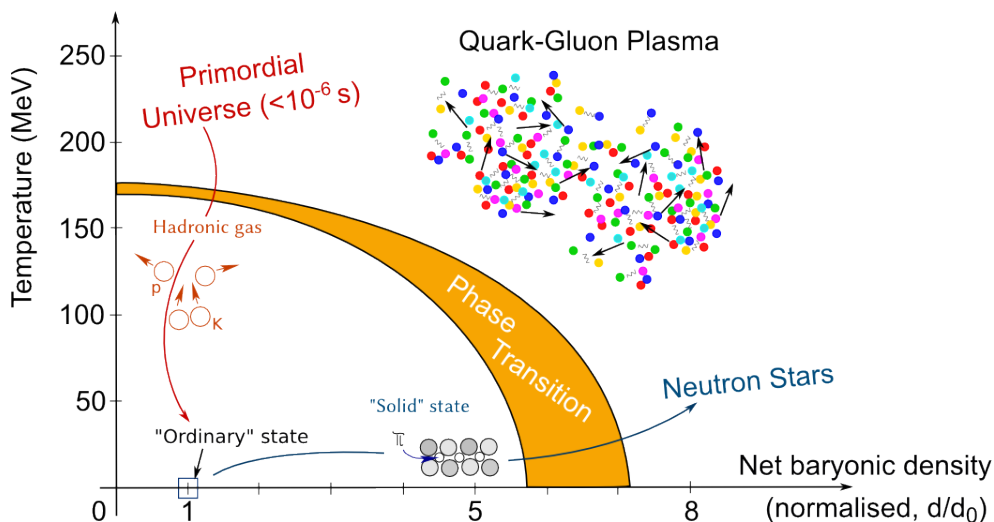


Figure 1.1: The phase diagram of quantum chromodynamic (QCD) matter [1] in the net baryonic density to temperature plane: At low temperatures and high densities neutron stars are expected.

Neutron stars are formed in the aftermath of the gravitational collapse of the core of a giant star heavier than 8 solar masses (M_{\odot}) [2] at the end of its lifetime, when all the nuclear fuel in its core is exhausted. This rapid collapse triggers a Supernova explosion in which neutron stars are born [2].

These stars represent some of the densest objects in the universe. Around 35 of the known neutron stars are found to have masses between 1.17 to $2.0 M_{\odot}$ and radii of 10 – 11.5 km [3]. The latter can be obtained by measuring the neutron stars space time effects on its detected thermal emission [3]. Due to gravity, their core region is compressed to more than twice the density of ordinary nuclear matter, which has an equilibrium value of $n_0 = 0.16 \text{ fm}^{-3}$.

In addition, the temperature in their core is relatively low, typically smaller than 1 MeV or 10^{10} K [4]. This features render them a perfect laboratory to study cold and dense matter, see Fig 1.1. At high temperatures and/or densities it is expected that matter transitions from the hadronic into a deconfined phase of quarks and gluons, called the quark-gluon plasma (QGP). Experimentally, the QGP is studied in relativistic heavy-ion collisions where high temperatures and densities are reached.

The outer crust of a neutron star is thought to consist of mostly nuclei and electrons [5]. Progressing inwards the density increases, which leads the electron Fermi energy to

increase as well and it becomes more favourable that electrons get captured by protons. The nuclei become more neutron rich and free neutrons appear at a density of $4 \cdot 10^8 \text{ kg/m}^3$ [5]. Further in, the nuclei decompose into their constituents and form a layer made of neutrons, protons and electrons in β -equilibrium [5]. But there are uncertainties about the composition of the ultra dense core region and inner layers of a neutron star. At certain densities neutrons begin to overlap geometrically and at even higher densities exotic forms of matter might appear.

Neutron Star matter can be characterized by its Equations of State (EoS), which relates pressure p to energy density ϵ . It depends on the particles that are present and how they interact with their surroundings. The EoS allows to derive macroscopic properties and to describe the structure of the neutron star. It solves the TOV equations of hydrostatic equilibrium, named after R. C. Tolman [6], J. R. Oppenheimer and G. M. Volkoff [7], who derived them from general relativity in 1939

$$\frac{dp}{dr} = -\frac{G_N (p + \epsilon)(m + 4\pi r^3 p/c^2)}{c^2 r^2 [1 - 2G_N m/(rc^2)]}, \quad (1.1)$$

$$\frac{dm}{dr} = 4\pi r^2 \frac{\epsilon}{c^2}, \quad (1.2)$$

where ϵ is the energy density, G_N Newton's gravitational constant, p the pressure, r the radius and m the enclosed mass. From this a mass-radius relation can be deduced, which allows to estimate the maximum neutron star mass an EoS can support, depending on its stiffness.

However, as the exact composition of the neutron star core is unknown and the EoS at such high densities presents uncertainties [3], different models have been suggested where each leads to a different EoS.

One possibility is the emergence of hyperons at densities around 2-4 n_0 due to weak interactions. This leads to an additional degree of freedom as hyperons contain strange quarks, which would typically soften the EoS and reduce the maximum reachable mass. Therefore, the presence of hyperons is not obviously compatible with heavy neutron stars with masses around $2 M_\odot$ [4], that have been discovered in the past decade. An example is the pulsar J0348+0432, which has a mass of $2.01 \pm 0.04 M_\odot$ [8]. The difficulty of how to connect the appearance of hyperons with this large neutron star masses is also known as *hyperon puzzle* and is one of the hot topics in astrophysics.

At the moment, is an ongoing effort to understand the hyperon-baryon (Y-B) interaction, see for example [9] or [10]. However, also hyperon-hyperon (Y-Y) interactions might play an important role to solve the puzzle. They are usually included in the EoS via the additional exchange of strange attractive scalar- (σ^*) and/or repulsive vector mesons (ϕ). The corresponding Lagrangian is the following [11]

$$\begin{aligned}
\mathcal{L}_{YY} = & \sum_B \bar{\Psi}_B (g_{\sigma^* B} \sigma^* - g_{\phi B} \gamma_\mu \phi^\mu) \Psi_B \\
& + \frac{1}{2} (\partial_\mu \sigma^* \partial^\mu \sigma^* - m_{\sigma^*}^2 \sigma^{*2}) \\
& - \left(\frac{1}{4} \phi_{\mu\nu} \phi^{\mu\nu} - \frac{1}{2} m_\phi^2 \phi_\mu \phi^\mu \right).
\end{aligned} \tag{1.3}$$

The first term describes the interaction between the particles of the full standard baryon octet ($J^P = \frac{1}{2}^+$) – including the nucleons and hyperons in the neutron star matter – and σ^* or ϕ respectively. The second one characterizes the scalar field with the corresponding kinetic and mass term and the last one the vector field. In order to obtain the stiffest EoS only the repulsive ϕ -meson, which is a nearly pure ($s\bar{s}$) state, is considered in Eq. 1.3. The Y-Y interaction via ϕ exchange is illustrated schematically in Fig. 1.2.

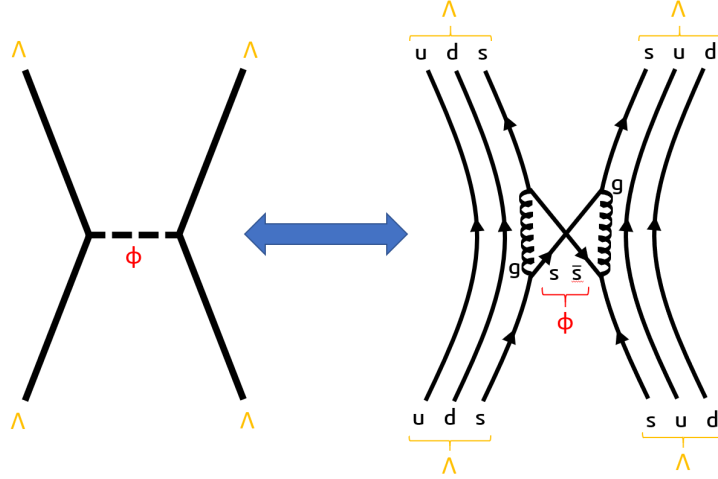


Figure 1.2: Schematic diagram of a Y-Y interaction – here two Λ s with valence quark content of (uds) – via the exchange of a ϕ -meson, which has a valence quark content of ($s\bar{s}$). The time axis is in vertical direction.

Figure 1.3 shows the mass radius relation of neutron stars for different Ξ single particle potentials U_Ξ within the relativistic mean field Model (RMF) [11]. In the lower branch of mass-radius relations only the exchange mesons σ , ω and ρ (model $\sigma\omega\rho$) are considered, while in the upper branch the ϕ -meson is included in the calculations (model $\sigma\omega\rho\phi$). Recent studies from the HAL QCD Collaboration in 2018 [12] predict a slightly repulsive Ξ single-particle potential with $U_{\Xi^-} \sim 6$ MeV/ c in pure neutron matter (PNM), which is found in neutron stars. Therefore, in Fig. 1.3 the two curves with $U_\Xi \sim 0$ MeV/ c are relevant. Whether or not the repulsive interaction is included gives very different results and has to be considered in order to determine a realistic EoS. The understanding of the ϕ coupling is essential and can be studied using the method of femtoscopy as scattering experiments are not possible due to the short lifetime of the particles of interest.

Concerning hyperons for example, it is simply not possible to create targets and also the formation of hyperon beams presents difficulties. Also, there are several recent studies where femtoscopy has been used successfully in order study baryon-baryon [13], [9] or baryon-meson interactions [14].

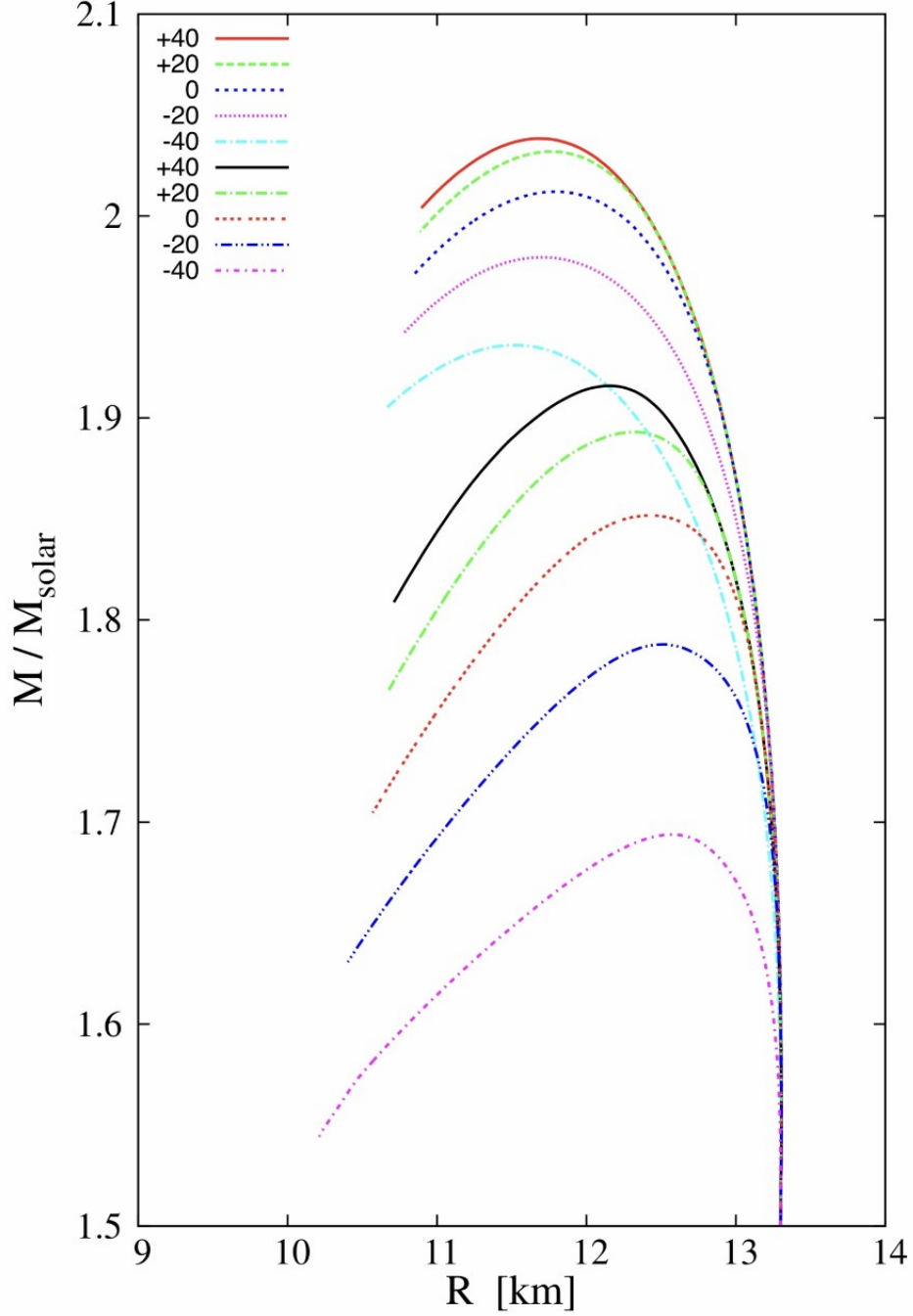


Figure 1.3: The mass-radius relation of neutron stars for different Ξ single-particle potentials. Upper branch: model $\sigma\omega\rho\phi$, lower branch: model $\sigma\omega\rho$ [11]

2 Femtoscopy

The system created in relativistic particle collisions has spatial extensions of a few femtometers $\sim 10^{-15}$ and evolves on time scales of $\sim 10^{-22}$ s. This makes it impossible to measure its properties directly. Instead, femtoscopy can be used to investigate the correlation of two final state particles emitted close to each other in position and momentum space.

Originally, femtoscopic correlations were mainly used to determine the properties of the particle emitting source in heavy ion collisions [15], where particles at low relative momenta undergoing a known interaction are analyzed. But not the size of the entire source is measured, rather the *region of homogeneity*, which is the dimension of the phase space cloud of outgoing particles with velocities of specific directions and magnitudes.

This paradigm, however, can be turned around. In systems where the emission of particles is well understood, femtoscopy enables the study of the strong final state interaction of pairs, when it is impossible to carry out traditional scattering experiments as mentioned before.

After the collision of two particles at high energies a fireball is formed that immediately expands and cools down while hadrons are formed. If two particles are emitted close to each other in the range of a few femtometers – as the strong interaction is short-ranged – they experience a final state interaction that modifies their relative momentum. This leads to a correlation signal. By further expanding and cooling down, the system reaches a point where there are no more interactions between hadrons, called thermal freeze-out. This means they can move to the detector undisturbed and the interaction can be measured via the correlation function $C(k^*)$. Here the $k^* = \frac{|\vec{p}_1^* - \vec{p}_2^*|}{2}$ denotes the relative momentum between both particles.

2.1 The correlation function

The ratio between the probability $P(\vec{p}_1, \vec{p}_2)$ of one particle having a momentum \vec{p}_1 while a second one with \vec{p}_2 was already emitted in the same event and the probability of finding particles with momenta \vec{p}_1 and \vec{p}_2 in separate events [16] leads to the two-particle correlation function. It can also be calculated by dividing the Lorentz-invariant two particle cross section by the product of the two single particle distributions [17]. Summarizing the correlation function is defined by

$$C(\vec{p}_1, \vec{p}_2) = \frac{P(\vec{p}_1, \vec{p}_2)}{P(\vec{p}_1)P(\vec{p}_2)} = \frac{E_1 E_2 dN / (d^3 p_1 d^3 p_2)}{(E_1 dN / d^3 p_1)(E_2 dN / d^3 p_2)} \quad (2.1)$$

If there is no correlation between the particles the correlation function is equal to unity, as the particles are independent and $P(\vec{p}_1, \vec{p}_2) = P(\vec{p}_1) \cdot P(\vec{p}_2)$.

2.1.1 Experimental Definition

To measure the correlation function experimentally the probabilities in Eq. 2.1 are replaced by the corresponding correlated and uncorrelated particle yields. The former is extracted by pairing the particles of interest from the same event, whereas the latter has to be extracted by using an event-mixing technique, pairing the particles of interest from different events, which renders them uncorrelated [18].

Equation (2.1) can be rewritten

$$C_{exp}(k^*) = \mathcal{N} \frac{N_{same}(k^*)}{N_{mixed}(k^*)}, \quad (2.2)$$

where \mathcal{N} is a normalization factor in order to $C_{exp}(k^*) \rightarrow 1$ for $k^* \rightarrow \infty$.

2.1.2 Theoretical Definition

A general equation that connects the measured correlation function to the space-time emission function $s(\mathbf{p}, \mathbf{x})$ using a convolution with the wave function Ψ reads as the following and is valid for any pairs [15]

$$C(\vec{P}, \vec{q}) = \frac{\int d^4\mathbf{x}_1 d^4\mathbf{x}_2 s_1(\mathbf{p}_1, \mathbf{x}_1) s_2(\mathbf{p}_2, \mathbf{x}_2) |\Psi(\vec{q}^*, \vec{r}^*)|^2}{\int d^4\mathbf{x}_1 s_1(\mathbf{p}_1, \mathbf{x}_1) \int d^4\mathbf{x}_2 s_2(\mathbf{p}_2, \mathbf{x}_2)}, \quad (2.3)$$

where $\vec{P} = \vec{p}_1 + \vec{p}_2$ is the total and $\vec{q} = \vec{p}_1 - \vec{p}_2$ the relative momentum vector of the pair, $s_i(\mathbf{p}_i, \mathbf{x}_i)$ describes the probability of emitting a particle with momentum and energy $\mathbf{p}_i = (E_i, \vec{p}_i)$ at a space-time point $\mathbf{x}_i = (t_i, \vec{x}_i)$ for $i = 1, 2$ and the squared relative two particle wave function serves as a weight. Stars denote quantities in the pair rest frame, also called the centre of mass frame where $\vec{p}_1 + \vec{p}_2 = 0 \rightarrow \vec{P} = 0$. Equation 2.3 can be further simplified following [15] and [19]:

$$C_{theo}(k^*) = \int d^3r^* |\Psi_{k^*}(\vec{r}^*)|^2 S(\vec{r}^*), \quad (2.4)$$

where $k^* = \frac{1}{2} \cdot |\vec{p}_1^* - \vec{p}_2^*| = \frac{1}{2} \cdot |\vec{q}^*|$ is the reduced relative momentum of the pair, \vec{r}^* the relative distance between the production points of the two particles and $S(\vec{r}^*)$ the source function, which describes the spatial probability density.

In femtoscopy it is often assumed that the spatial distribution has the shape of a Gaussian with width r_0 and there are neither explicit time nor momentum dependencies. The corresponding Gaussian two-particle source function is of the following form:

$$S_G(\vec{r}^*) = (4\pi r_0^2)^{-3/2} \cdot \exp\left(-\frac{r^{*\ 2}}{4r_0^2}\right) \quad (2.5)$$

Different forms of interactions are responsible for the final form of the correlation signal, for example Coulomb interaction for charged particles and/or strong interaction for hadrons. For identical particles quantum effects due to the Pauli-exclusion principle have to be considered, as the wave function is anti-symmetric for fermions and symmetric for bosons.

2.2 Lednicky Model

To extract information about the interaction from the measured data one needs to model the correlation function. R. Lednicky and V. L. L. Lyuboshitz derived an analytical approach to model the correlation function for strong final state interactions with an isotropic source of finite lifetime and Gaussian profile, Eq. 2.5, within the effective range expansion. The Lednicky model takes the scattering length and effective range of the interaction as input and by fitting the measured correlation function one can determine these parameters. For interacting particles the emission amplitude is the following [20]

$$\Psi_{p_1,p_2}(x_1, x_2) = e^{iP(x_1+x_2)/2}(e^{iq(x_1-x_2)/2} + \phi_{p_1,p_2}(x)), \quad (2.6)$$

where $P = p_1 + p_2$ and $q = p_1 - p_2$. The first term of the sum in Eq. 2.6 is the incoming plane wave and the second term the scattered wave. If the intrinsic length of the interaction potential is small compared to the distance r^* in the pair rest frame, the following approximation is valid [20]

$$\phi_{p_1,p_2}(x) = f(k^*)\Phi_{p_1,p_2}(x), \quad (2.7)$$

where $f(k^*)$ denotes the scattering amplitude. By neglecting effects of the potential on the wave function, $\Phi_{p_1,p_2}(x)$ takes the form of a diverging spherical wave

$$\Phi_{p_1,p_2}(x) = \frac{e^{ik^*r^*}}{r^*} \quad (2.8)$$

and the complex scattering amplitude in the effective range approximation can be written as [20]

$$f(k^*) = \left(\frac{1}{f_0} + \frac{1}{2}d_0k^{*2} - ik^* \right)^{-1}, \quad (2.9)$$

where f_0 is the scattering length and d_0 the effective range. From this a theoretical correlation function can be determined. For uncharged particles it reads [20]

$$C(k^*) = 1 + \sum_S \rho_S \left[\frac{1}{2} \left| \frac{f(k^*)^S}{r_0} \right|^2 \left(1 - \frac{d_0^S}{2\sqrt{\pi}r_0} \right) + \frac{2\Re(f(k^*)^S)}{\sqrt{\pi}r_0} F_1(q^*r_0) - \frac{\Im(f(k^*)^S)}{r_0} F_2(q^*r_0) \right], \quad (2.10)$$

where the sum is over all possible spin states, ρ_S is the pair fraction emitted into a certain spin state S , $F_1(q^*r_0)$ and $F_2(q^*r_0)$ denote analytical functions from the approximation of the source with a Gaussian profile. The analytical correlation function can be used to fit the actual correlation function. From this it is possible to obtain the scattering parameters corresponding to the interaction between the particles.

2.3 CATS

The Correlation Analysis Tool using the Schrödinger equation, short CATS, is a program written in C++ to numerically compute the two particle correlation function and it is used to fit the experimental results of an analysis. One can use any type of source function or interaction potential and get the corresponding wave function. Compared to the Lednicky model it does not use any expansions but calculates the exact solution of the wave function and one has the flexibility to decide over the source function and potential. More details can be found in [21].

2.4 Corrections

There are three categories of corrections to the correlation function that need to be accounted for: finite momentum resolution, non femtosopic background and mis-identified particles [15]. In the following they will be discussed in more detail.

The finite single-track momentum resolution of the detector is typically of the order of 1% and blurs the correlation function. It can be corrected comparing the true generated relative momentum k_{gen}^* from Monte Carlo simulated data with the reconstructed one k_{rec}^* from actual data. From this, one gets the smeared momentum matrix, which is then multiplied to the correlation function.

Non-femtoscopic background leads to an additional signal in the function for $k^* > k_{\text{femto}}^*$ where the correlation function would be expected to approach unity as k_{femto}^* , typically around 200 MeV/c, is the upper limit of the relative momentum where the particles are sensitive to final state interactions. The background is typically fitted as linear baseline [15]

$$C(k^*)_{\text{non-femto}} = a \cdot k^* + b, \quad (2.11)$$

where a and b are parameters. The non-femtoscopic background modifies the correlation function as $C(k^*) = C_{\text{femto}} \cdot C_{\text{non-femto}}$. It is thought to originate from energy momentum conservation and can have different sources. For example correlations due to the emission of jet-like shapes will induce a signal and are often referred to as mini-jets. Therefore, studying the event properties is crucial, see Section (4.1.1).

Mis-identified and secondary-particle contamination might also contribute to the correlation signal. It is usually assumed that mis-identified particles or impurities are uncorrelated. This residuals are assumed to be flat and thus just damp the correlation signal [15].

But there is also correlated contamination due to the fact that some identified particles are not primaries but secondaries originating from decays of resonances, also called feed-down.

These effects induce a fake pair correlation signal and are accounted for with λ parameters: If these particle pairs originate from the relevant region to the correlation, the

signal gets altered by the factor λ . This leads to a modified correlation function of [9]

$$C_{femto}(k^*) = 1 + \lambda_{\text{real}} \cdot (C_{\text{real}}(k^*) - 1) + \sum_{ij} \lambda_{ij} (C_{ij}(k^*) - 1), \quad (2.12)$$

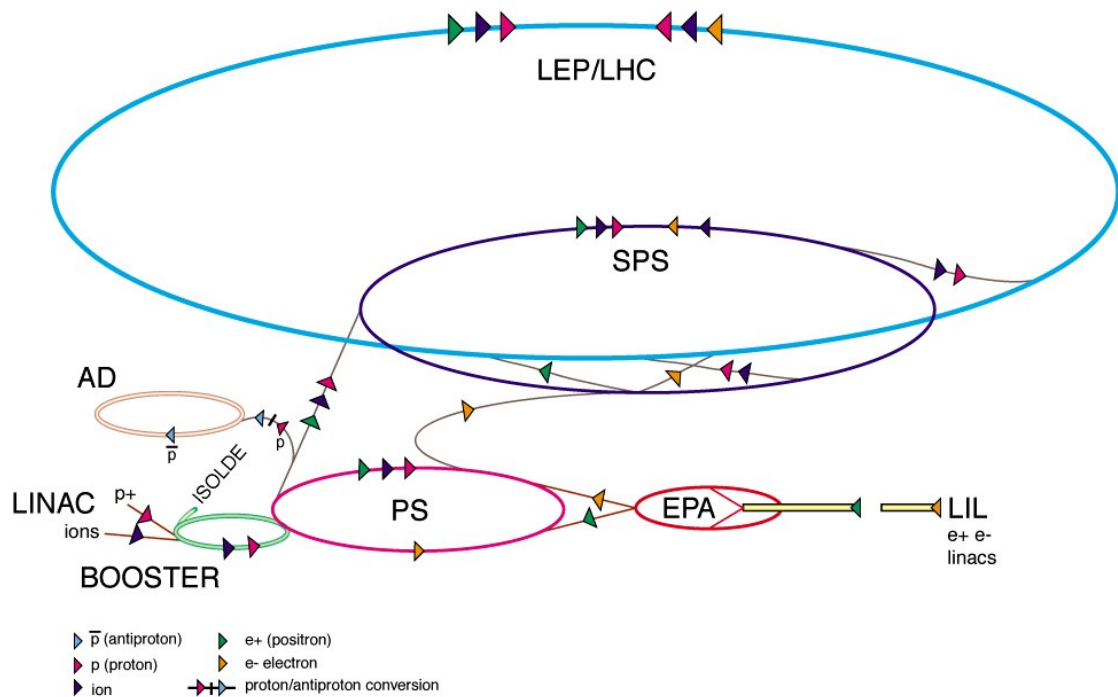
where the sum is over all possible impurities and secondary-particle contaminations. All λ parameters are calculated the following way

$$\lambda_{ij} = \lambda_i \cdot \lambda_j = P_i f_i \cdot P_j f_j, \quad (2.13)$$

where P is the purity of the particles and f the fraction of particles originating from a specific long-lived decay channel, while for λ_{real} the primary fraction is considered.

3 Experimental Setup

3.1 The LHC



CENR AC_HF205_V2/2/1998

Figure 3.1: The CERN accelerator complex [22]

The Large Hadron Collider (LHC) is a hadron accelerator and collider. It was built in the already existing tunnel of the Large Electron-Positron collider (LEP) at CERN, the European Organization for Nuclear Research, and has a circumference of 26.7 km. The LHC is a particle-particle collider, therefore, it has two rings with beams that rotate in the opposite direction. Either protons or heavy ions (Pb and more recently also Xe) are used. There are eight beam interaction points, but only four are used for experiments in order to prevent unnecessary disruptions of the beam. The experiments are ATLAS, CMS, ALICE and LHCb.

Beam protons are injected from the Linac2 accelerator chain which consists of the Linac2 itself, which contains the proton source, the Proton Synchrotron Booster (PSB), the

Proton Synchrotron (PS) and the Super Proton Synchrotron (SPS). The whole acceleration process is depicted in Fig. 3.1.

At the LHC twin bore magnets are used due to space limitations. They are superconducting and cooled to a temperature of 2 K using technology based on NbTi Rutherford cables [23].

3.2 The ALICE Experiment

The data of this analysis is from proton-proton collisions at $\sqrt{s} = 13$ TeV provided by A Large Ion Collider Experiment (ALICE). Its main task is to investigate the properties of the quark-gluon plasma and general strongly interacting matter. In addition to A-A collisions also A-p and pp collisions are detected, where A can be lead (Pb) or xenon (Xe).

The schematic setup of ALICE is shown in Fig.(3.2). The so-called central barrel is embedded in a large solenoid magnet, which stems from the L3 experiment at LEP. Its onion-like structure is built in the following way: Located around the beam pipe there is the Inner Tracking System (ITS), which is a silicon tracker. Progressing outwards there comes the cylindrical, gas-filled Time Projection Chamber (TPC). Next comes the Transition Radiation- (TRD), the Time of Flight- (TOF) and the Ring Imaging Cherenkov- (HMPID) detector followed by the calorimeters PHOS and EMCal. The ACORDE scintillators on top of the big magnet are installed to trigger on cosmic radiation. In the following sections the ITS, TPC and TOF are explained in more detail.

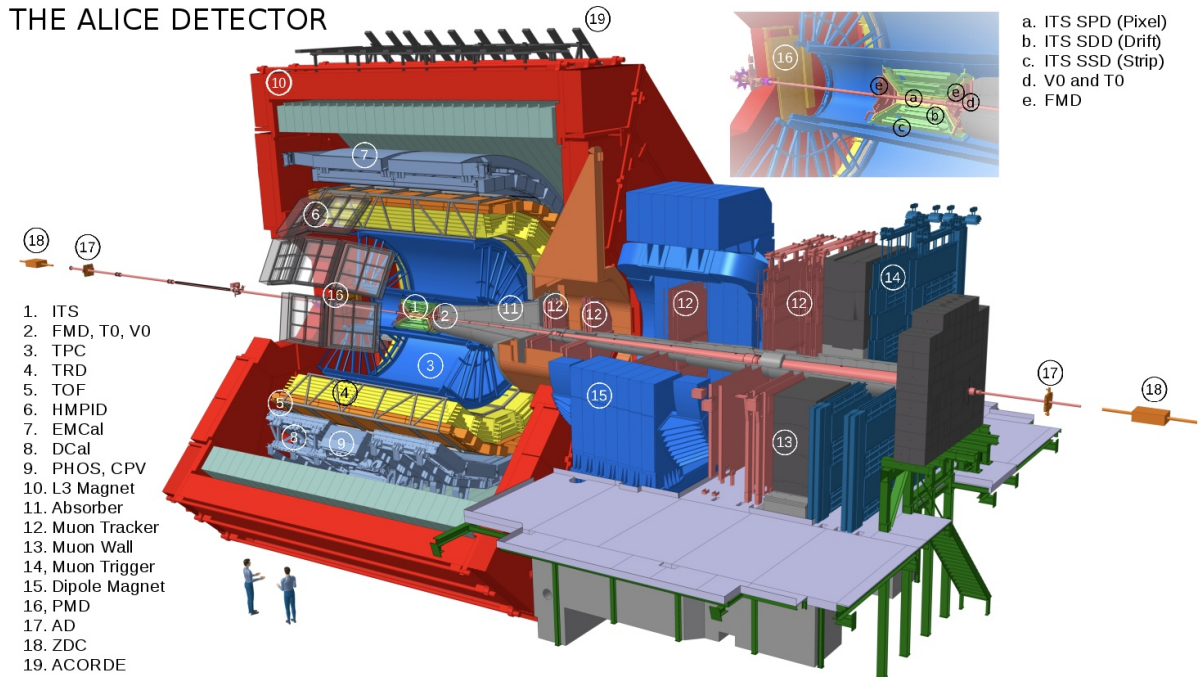


Figure 3.2: The ALICE schematic layout [24]

3.2.1 Inner Tracking System (ITS)

The ITS is the innermost part of the detector and surrounds the beam pipe. It is made of six layers of cylindrical silicon detectors which lie between a radius of 3.9 cm and 43 cm from the interaction point [25]. The ITS covers a pseudorapidity range of at least $|\eta| < 0.9$ depending on the detector [25] and has a spatial precision of $\mathcal{O}(10 \mu\text{m})$ [26].

The two innermost layers consist of **Silicon Pixel Detectors** (SPD). Their main purpose is to determine the primary vertex position and to measure the tracks of secondaries from decays of particles consisting of the three heavy quarks. It operates in regions of high radiation levels and track densities of $\sim 50 \text{ tracks/cm}^2$.

Radially outward follow two intermediate layers of **Silicon Drift Detectors** (SDD). They are used for the ITS particle identification as they provide information about the energy loss dE/dx and have a good multi-track capability.

Last there are two outer layers of **Silicon Strip Detectors** (SSD). They measure the energy loss dE/dx of low momentum particles $< 200 \text{ MeV}/c$.

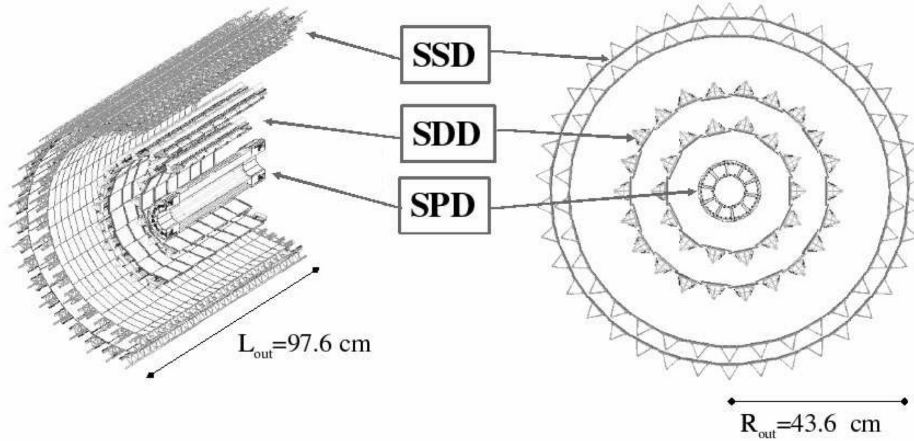


Figure 3.3: The ALICE ITS [26]

3.2.2 Time Projection Chamber (TPC)

The TPCs' main purpose is to measure charged-particle momenta with good track-separation, vertex determination and particle identification. It is the main tracking device of ALICE and is located between 84 cm and 2.47 m in radial direction from the interaction point. It covers a pseudorapidity of $|\eta| < 0.9$, the full azimuth – beside dead zones between neighboring readout chambers – and a large p_T range from 0.1 to $100 \text{ GeV}/c$ [24]. The TPC has a cylindrical shape and is made of a large field cage of 90 m^2 filled with 90 % Ne and 10 % CO_2 [27]. At the end of the TPC cylinder the inner and outer readout chambers are located. They are both equipped with multi-wire proportional chambers (MWPCs) with slightly different wire geometry. The inner

one consists of 63 and the outer one of 96 pad rows, which makes a total of 159 rows and about 560,000 readout pads in order to keep a low occupancy and have a high resolution [24].

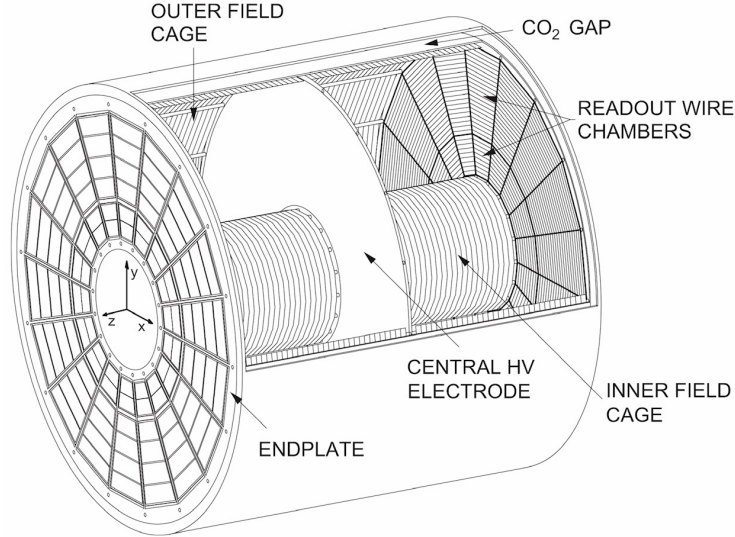


Figure 3.4: The ALICE TPC [24]

The field cage assures a uniform electrostatic field in the gas volume, which transports electrons, stemming from the ionized gas from charged particles traversing the detector, to the readout chambers without any significant perturbation.

Each chamber consists of three wires and a pad plane: Next to the pad plane, there is the anode grid where the electrons ionize the gas creating an avalanche amplification. This causes a positive current signal in the wires (fast rise time, long tail) which is read out by the pad planes. Next comes the cathode grid that separates the amplification from the drift-volume and catches most of the ions created in the avalanche. Last there is the gating grid that stops ions created in the avalanche process to move back into the drift volume, which could cause severe perturbations of the drift field. It is normally closed and opens only for the duration of one drift-time interval of about $90 \mu\text{s}$ upon a trigger signal [24]. Due to the high spatial resolution of the TPC the position of the original particle interaction with the drift gas by ionization can be reconstructed and thus the particle track as well. During the TPC upgrade from 2019 to 2021 the MWPCs are replaced with Gas Electron Multipliers (GEMs) which make a continuous read out possible, as they do not use a gating grid.

The particle momentum can be determined from its bending radius due to the magnetic field by measuring each space-time ionization event. This observable together with the specific energy loss makes it possible to identify particles. The specific energy loss of the

particle due to collisions with the drift gas molecules measured with the TPC is shown in Fig. 3.5. It is related to the Bethe Bloch formula [28]

$$-\frac{dE}{dx} = \frac{4\pi n z^2}{m_e c^2 \beta} \left(\frac{e^2}{4\pi\epsilon_0} \right)^2 \left[\ln \left(\frac{2m_e c^2 \beta^2}{I \cdot (1 - \beta^2)} \right) - \beta^2 \right], \quad (3.1)$$

with $\beta = \frac{v}{c}$, ze the charge and v the speed of the particle, n the electron number density and I the mean excitation level. The quality of the particle identification gets expressed by n_σ , which is the number of standard deviation of the measured energy loss of a particle to the expected value for a certain particle type expressed in terms of the detector resolution [25]

$$n_{\sigma,\text{particle}} = \frac{dE/dx - \langle dE/dx \rangle}{\sigma_{dE/dx}}. \quad (3.2)$$

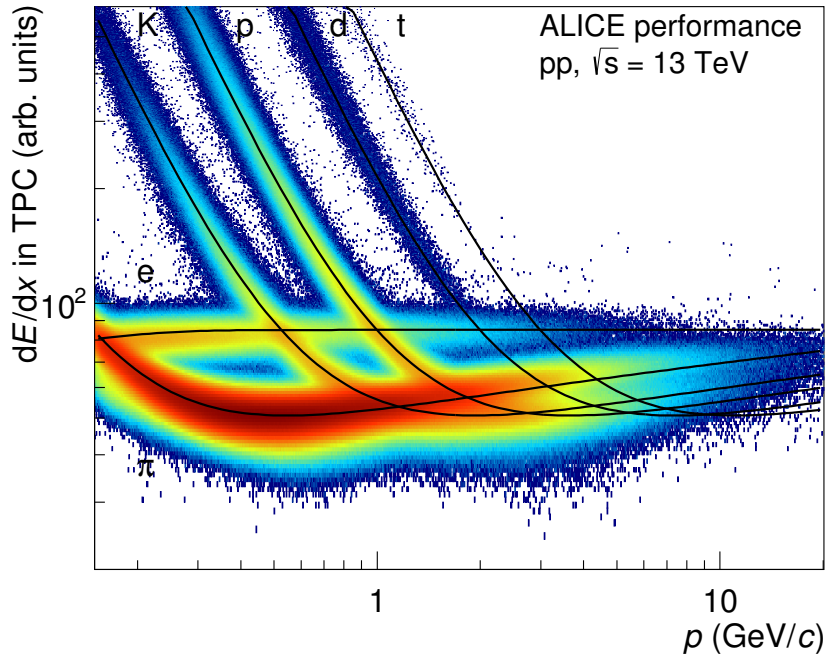


Figure 3.5: The TPC energy loss as a function of the momentum p [29]

3.2.3 Time Of Flight Chamber (TOF)

The TOF detector is a large area array of Multigap Resistive Plate Chambers (MRPC) between 3.70 and 3.99 m from the beam axis. Like the TPC it covers the full azimuth and a pseudo-rapidity range of $|\eta| < 0.9$ and is used for particle identification (PID) in the intermediate momentum range. It completes the track reconstruction and energy

loss measurement from ITS and TPC for low momenta $< 1 \text{ GeV}/c$. The TOF is divided into 18 sectors, covering a cylindrical surface of polar acceptance $< 45^\circ$ [26].

The MRPCs have a high and uniform electric field so that there is an immediate electron avalanche from any ionization due to a charged particle traversing the chamber. The T0 detector provides the start time of the event t_{event} and consist of an array of Cerenkov counters at each side of the interaction point [25]. Besides this also arrival times of the particles at the TOF detector are estimated and used as t_{event} in case the T0 signal is not present. By measuring the time of flight particles can be identified. Figure 3.6 shows the measured velocity β distribution as function of the momentum p .

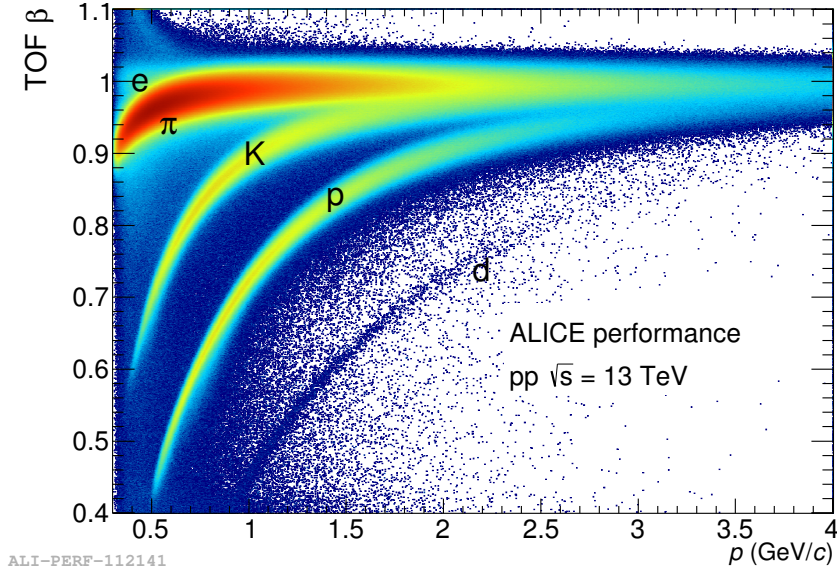


Figure 3.6: β distribution measured with the TOF detector as a function of the TPC-momentum [30]

3.3 Track reconstruction

To find and fit the tracks the Kalman filter is used, which depends on initial seed values for the track parameters and the corresponding covariance matrix [26]. This values are determined for each pad row of the TPC by using reconstructed space points of the TPC, once under the constraint of the primary vertex position reconstructed from the ITS and once under the assumption that the track comes from another point. If there is one space point matching the prolongation of the track it is added to the measurement and the matrix and track parameters get updated. The track is then propagated to the ITS. If there are more than one possible matching space points, each of them is followed separately towards the innermost layer of the ITS and the best fitting track is used in the end.

After the completed ITS tracking, the track is followed from the innermost layer of the ITS outwards, starting with more precise parameters. After the ITS the track is followed

through the TPC matching the tracks with the outer detectors like the TRD and TOF. Finally, the Kalman filter is reversed another time and tracks are fitted again from the outside to the innermost layer, in order to get the most precise parameter values near the primary vertex.

3.4 AliRoot

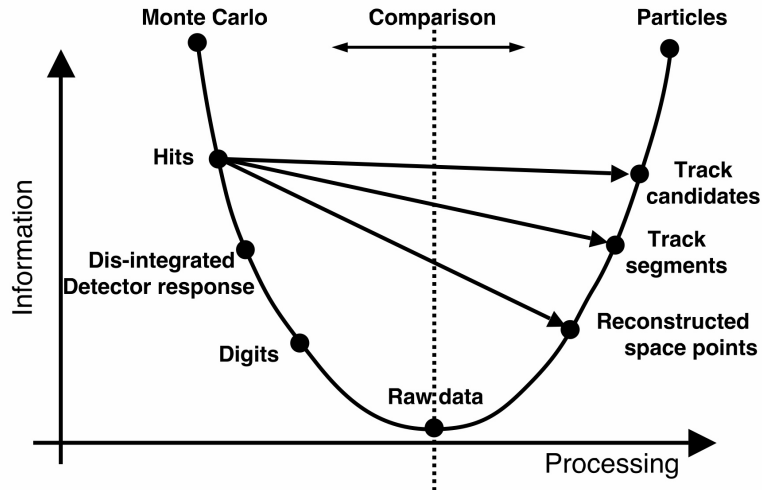


Figure 3.7: The AliRoot processing framework [26]

The AliRoot framework is based on object-orientated programming techniques and entirely written in C++ [26]. It is an addition to the Root system and part of the AliEnv. The latter gives access to the Worldwide LHC Computing Grid (WLCG), which is a global collaboration of computer centres that provide a possibility to store, analyze and distribute the LHC data [31]. It is possible to replace some well defined parts of the AliRoot system by implementing own code without any impact on the rest.

Figure 3.7 shows the data processing framework. Event generators like PHYTIA produce the physics processes at parton level. The data contains type, momentum, charge and parent-child relationships of the generated particles and for each of the crossing particles the detector response is simulated. The corresponding energy deposition for a given space-time point is saved in so called hits. Together with the detector response they are combined to digits which are stored in each detector. The reconstructed particles and their tracks are then compared to the generated ones. The data is stored in the form of Event Summary Data (ESD) which include global event properties and lists of reconstructed particles and tracks. The reduced Analysis Object Data (AOD) contains sufficient information for common analyses and is produced from ESD. It has a filterbit mask which corresponds to a given set of cuts in order to have quality tracks. In this analysis NanoAODs are used, which are even more lightweight than normal AODs as they contain the minimal amount of information needed for a femtoscopic analysis.

4 Data Analysis

4.1 Event selection

In this analysis data from proton-proton collisions at $\sqrt{s} = 13$ TeV is used, which includes the whole data sets from 2016, 2017 and 2018. To select events suitable for the analysis, the recommended event cuts for Run 2 have been applied, see Table 4.1. In order to have events with only one pp collision per bunch crossing, pile-up, which includes additional pp interactions from the same bunch, is rejected. Both minimum bias (MB) and high multiplicity (HM) events are studied. The former uses a trigger (`kINT7`) with as little bias as possible and no pre-selection, while the latter triggers only events with high multiplicities (`kHighMultV0`). This can be seen in Fig. 4.1 that shows the relative amplitude measured at the V0 detector, which is proportional to the multiplicity, for minimum bias and high multiplicity events. Also more strangeness containing particles are produced for high multiplicity data, see Fig. 4.2. For this analysis HM is therefore the better choice, as the statistics are better due to an increased ϕ production. After event selection, there are $1.6 \cdot 10^9$ MB and $950 \cdot 10^6$ HM events at disposal for the analysis.

Table 4.1: Recommended event cuts Run 2

selection criteria	value
Trigger	<code>kHighMultV0</code> (for high multiplicity events) or <code>kINT7</code> (for minimum bias events)
Physics selection	default
Incomplete DAQ	check
z vertex	$ \text{vtx}_z < 10$ cm
Contributors to track vertex	$N_{\text{contrib,track}} > 1$
Contributors to SPD vertex	$N_{\text{contrib,SPD}} > 0$
Distance track and SPD vertex	$d_{\text{vtx,track-SPD}} < 0.5$ cm
SPD vertex z resolution	$\sigma_{\text{SPD,z}} < 0.25$ cm
Pile-up rejection	<code>AliEvent::IsPileUpFromSPD()</code> <code>AliEventUtils::IsSPDClusterVsTrackletBG()</code>

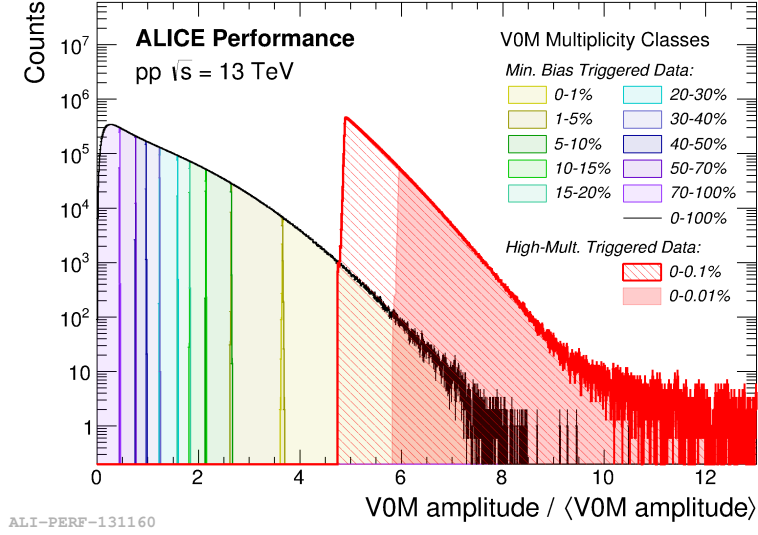


Figure 4.1: Distribution of the V0M amplitude scaled by its mean value, which is proportional to the event multiplicity. For MB events there is no pre-selection, while HM triggers only on high event multiplicities [32]

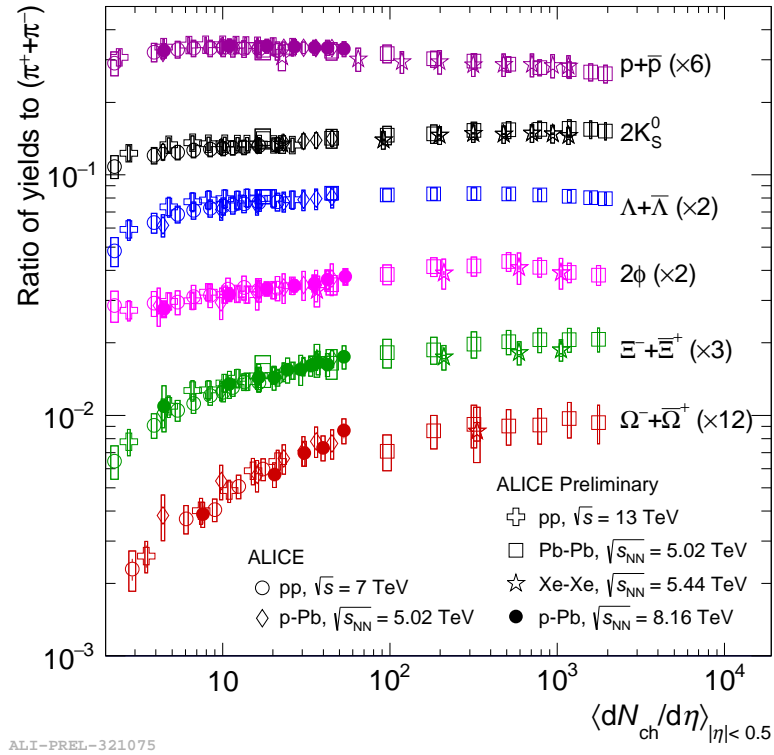


Figure 4.2: Particle-to-pion ratio as a function of multiplicity for different systems. The production of ϕ s increases with multiplicity. For protons it slightly decreases but the overall yield remains significantly larger than the ϕ [33]

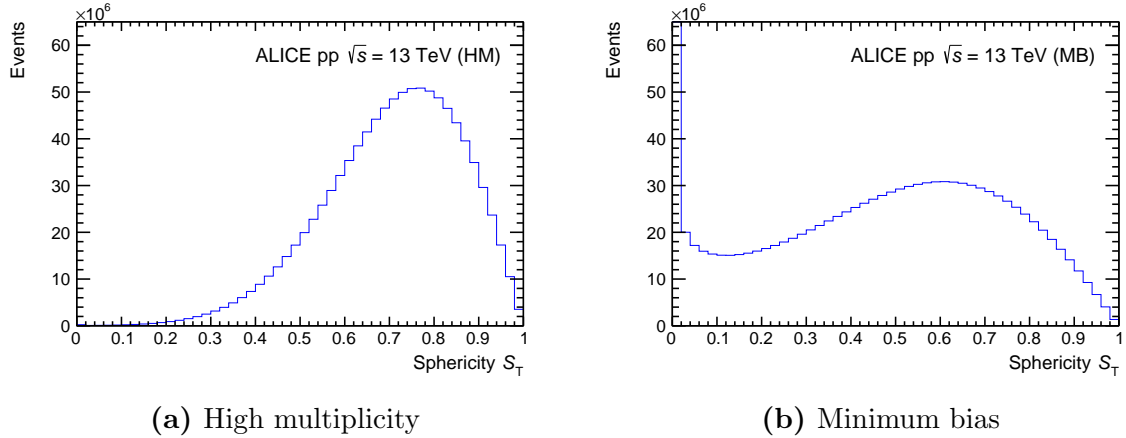


Figure 4.3: Sphericity distribution for high multiplicity and minimum bias events

4.1.1 Event shape

The ϕ -proton correlation function is sensitive to residual auto-correlations. In order to suppress the arising mini-jet background below ~ 1 GeV/ c , cuts on the event shape – which gives information about the properties of the hadronic final states after the particle collision – are needed. Mini-jets from low momentum transfer scatterings induce a correlation signal and it is believed that they originate from the incoherent fragmentation of multiple parton-parton scattering [34]. Two different event-shape properties, both defined in the transverse plane in order to avoid the bias from the boost along the beam axis [35], have been studied in this analysis: sphericity and sphericity.

Sphericity

To calculate the transverse sphericity of an event, following [36], one needs to diagonalize the transverse momentum matrix

$$\mathbf{S}_{xy} = \frac{1}{\sum_j p_{Tj}} \sum_i \frac{1}{p_{Ti}} \begin{bmatrix} p_{xi}^2 & p_{xi}p_{yi} \\ p_{yi}p_{xi} & p_{yi}^2 \end{bmatrix} \quad (4.1)$$

to get the eigenvalues λ_1 and λ_2 , with $\lambda_1 > \lambda_2$. The transverse sphericity is defined as the following

$$S_T = \frac{2\lambda_2}{\lambda_1 + \lambda_2}. \quad (4.2)$$

From previous analyses a sphericity cut of $0.7 < S_T < 1.0$ has been shown to be effective in reducing the background [14]. The corresponding distribution for HM events can be seen in Fig. 4.3a and the one for MB events in Fig. 4.3b. The HM seems to be more spherical and the resulting event yield is $525 \cdot 10^6$ for HM and $240 \cdot 10^6$ for MB.

Sphericity

The transverse sphericity is calculated the following way [37]

$$S_0 = \frac{\pi^2}{4} \min_{\vec{n}=(n_x, n_y, 0)} \left(\frac{\sum_i |p_{\perp, i} \times \vec{n}|}{\sum_i p_{\perp, i}} \right)^2, \quad (4.3)$$

where the unit transverse vector \vec{n} that minimizes the ratio is used. The distribution for HM events for $0.7 < S_0 < 1.0$ is shown in Fig. 4.4 and has a event yield of $306 \cdot 10^6$.

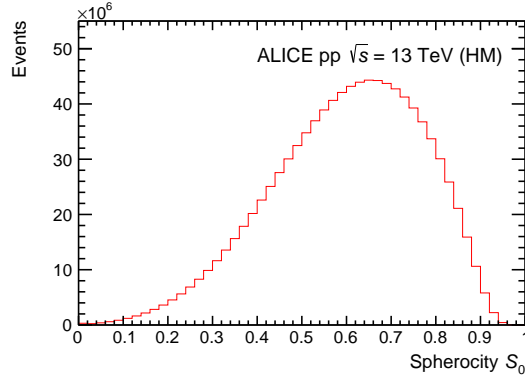


Figure 4.4: Sphericity distribution for high multiplicity events

Comparison

Both S_T and S_0 can take values between 0 and 1, where 0 corresponds to a jet-like event, in the shape of a pencil and 1 to a circularly symmetric event. By comparing the sphericity distribution with the sphericity distribution for HM events, one can see that the latter has overall less spherical events > 0.9 . The peak is shifted to smaller values compared to sphericity and is also wider. This shows that sphericity is in general the stricter observable, but accordingly rejects almost twice as many events as the sphericity.

4.2 Particle selection

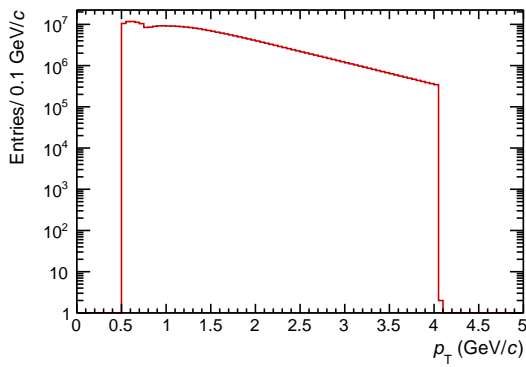
4.2.1 Proton candidates

Table 4.2: Primary Proton cuts

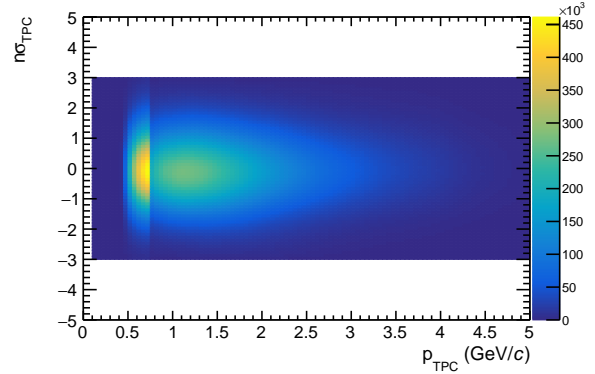
selection criteria	value
Filterbit	128 (TPC only tracks)
Pseudorapidity	$ \eta < 0.8$
Transverse momentum	$0.5 \text{ GeV}/c < p_T < 4.05 \text{ GeV}/c$
TPC Clusters	$N_{\text{TPC}} > 80$
Crossed TPC pad rows	$N_{\text{crossed}} > 70$
Findable TPC clusters	$N_{\text{crossed}}/N_{\text{findable}} > 0.83$
Tracks with shared TPC clusters	rejected
Distance of closest approach xy	$ DCA_{xy} < 0.1 \text{ cm}$
Distance of closest approach z	$ DCA_z < 0.2 \text{ cm}$
Particle identification	$ n_{\sigma,\text{TPC}} < 3$ for $p_{\text{TPC}} < 0.75 \text{ GeV}/c$ (TPC only) $n_{\sigma,\text{combined}} < 3$ for $p_{\text{TPC}} > 0.75 \text{ GeV}/c$ (TPC+TOF)

The cuts used to reconstruct primary protons are summarized in Table 4.2 and are following [9]. The distance of closest approach from the trajectory to the primary vertex in the beam (z) and transverse plane (xy) is the main observable to select primary particles and a transverse momentum range between $0.5 \text{ GeV}/c$ and $4.05 \text{ GeV}/c$ is chosen, see Fig. 4.5a. The upper bound is applied to increase the purity of the reconstructed particles and the lower bound to reduce the proton fraction originating from interactions of primary particles with the detector material. The yield drops slightly around $p_T = 0.75 \text{ GeV}/c$, which is due to the fact that for particle identification (PID) above $p_{\text{TPC}} = 0.75 \text{ GeV}/c$ also the TOF is used, while for smaller p_{TPC} only the PID selection provided by the TPC is applied with $|n_{\sigma,\text{TPC}}| < 3$, illustrated in Fig. 4.5b.

This momentum cutoff is chosen because for higher momenta the separation power of the TPC detector between the energy loss of protons and other particles decreases, which leads to mis-identifications and a reduced purity of the proton sample. In order to still identify protons with higher momenta a combination of TPC and TOF is used with $n_{\text{combined}} := \sqrt{(n_{\sigma,\text{TPC}})^2 + (n_{\sigma,\text{TOF}})^2} < 3$. The protons have a purity about 99 % in both HM and MB and the total yield consists of 87 % primaries and 13 % secondaries from weak decays of resonances, where Λ is the main source with a contribution of ~ 9 % of the total proton yield [9].



(a) Transverse momentum distribution



(b) $n_{\sigma, \text{TPC}}$ distribution

Figure 4.5: Transverse momentum (left) and nSigma (right) distribution of proton candidates for high multiplicity events

4.2.2 ϕ -meson candidates

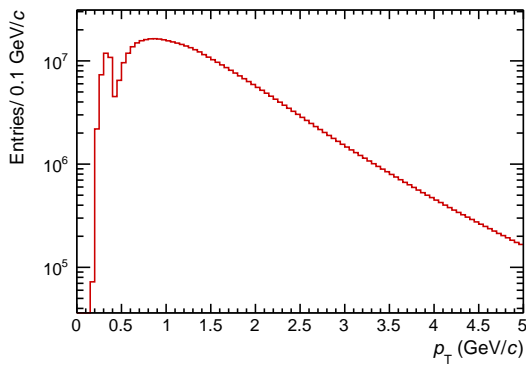
The ϕ -meson is an uncharged vector meson in a nearly pure ($s\bar{s}$) state with $J^P = 1^-$, a mass of $m = (1019.461 \pm 0.016)$ [38] MeV/c^2 and a full width of $\Gamma = (4.249 \pm 0.013)$ MeV [38]. From the relation $\Gamma = \hbar/\tau$ a lifetime of $\tau_\phi \sim 1.55 \cdot 10^{-22}$ s can be calculated. Its short lifetime in addition to its charge neutrality makes it impossible to detect the ϕ itself. Therefore, the vector meson can only be reconstructed due to its decay products using the method of invariant mass [28]

$$M_\phi^2 c^4 = p_\phi^2 c^2 = \left(\sum_i \mathbf{p}_i c \right)^2 = \left(\sum_i E_i \right)^2 - \left(\sum_i \vec{p}_i c \right)^2, \quad (4.4)$$

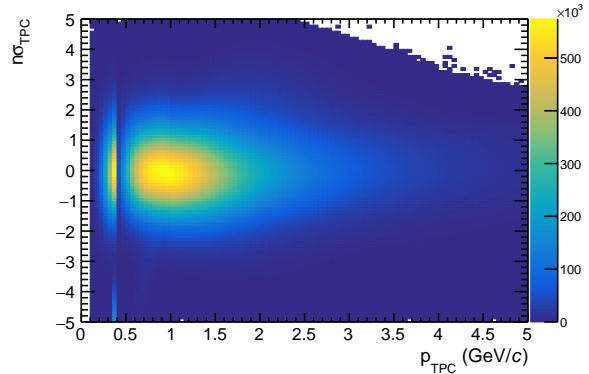
where the sum is over the products of one specific decay mode. The most probable one and easiest to reconstruct is the strong decay $\phi \rightarrow K^+ K^-$ with a branching ratio of $\text{BR}_{\phi \rightarrow K^+ K^-} = (49.2 \pm 0.5)\%$ [38]. This channel is also favoured by the Zweig rule, which states that processes with continuous quark lines in the Feynman diagrams are more common [28]. As it is a two-body decay Eq. 4.4 becomes

$$M_\phi^2 c^4 = m_1^2 c^4 + m_2^2 c^4 + 2(E_1 E_2 - |\vec{p}_1| |\vec{p}_2| c^2 \cos \theta), \quad (4.5)$$

where θ denotes the angle between \vec{p}_1 and \vec{p}_2 .



(a) Transverse momentum distribution



(b) $n_{\sigma,TPC}$ distribution

Figure 4.6: Transverse momentum (left) and nSigma (right) distribution of K^+ candidates for high multiplicity events

Kaon candidates

Table 4.3: Kaon cuts

selection criteria	value
Filterbit	96 (global tracks)
Pseudorapidity	$ \eta < 0.8$
Transverse momentum	$0.15 \text{ GeV}/c < p_T$
TPC Clusters	$N_{TPC} > 80$
Crossed TPC pad rows	$N_{crossed} > 70$
Findable TPC clusters	$N_{crossed}/N_{findable} > 0.80$
Tracks with shared TPC clusters	rejected
Distance of closest approach xy	$ DCA_{xy} < 0.1 \text{ cm}$
Distance of closest approach z	$ DCA_z < 0.2 \text{ cm}$
Particle identification	$ n_{\sigma,TPC} < 5$ for $p_{TPC} < 0.4 \text{ GeV}/c$ (TPC only)
	$n_{\sigma,combined} < 5$ for $p_{TPC} > 0.4 \text{ GeV}/c$ (TPC+TOF)

In order to reconstruct kaons, cuts following [39] are applied, which are summarized in Table 4.3. A lower limit of $p_T = 0.15 \text{ GeV}/c$ for the kaon transverse momenta is applied and the corresponding distribution for high multiplicity K^+ is shown in Fig. 4.6a. To identify the kaon candidates below $p_{TPC} = 0.4 \text{ GeV}/c$ only the TPC is used, while for larger momenta the PID information from TPC and TOF is combined, as in this momentum region the separation power of the TPC alone is not sufficient to distinguish kaons from other particles. This also causes a drop in the transverse momentum distribution around $p_T = 0.4 \text{ GeV}/c$, as already mentioned in Section 4.2.1. A relatively large $n_{\sigma,TPC}$ interval is chosen, see Fig. 4.6b, in order to reconstruct as many ϕ s as possible. For example, looking at minimum bias data, without applying any event shape cuts, a

significantly stricter selection on the kaon PID decreases the ϕ yield by $\sim 40\%$, while improving the purity only by $\sim 1\%$.

To investigate the particle purity, it is possible to use generated MB data, as the Monte Carlo Simulation has the advantage that all properties and identities of the particles are known. By applying the analysis on the generated data, the true particle type can be accessed. So it is possible to determine the purity of the kaons by comparing the identified ones with the correct ones. The K^+ and K^- purities are shown in Fig. 4.7 and are found to be consistent with each other. There is almost no contamination due to mis-identified particles for small transverse momenta, while for large p_T the kaon purity declines to $\sim 75\%$ due to the fact that the separation power of the TOF decreases significantly for kaons with a momentum higher than $p > \sim 1 \text{ GeV}/c$.

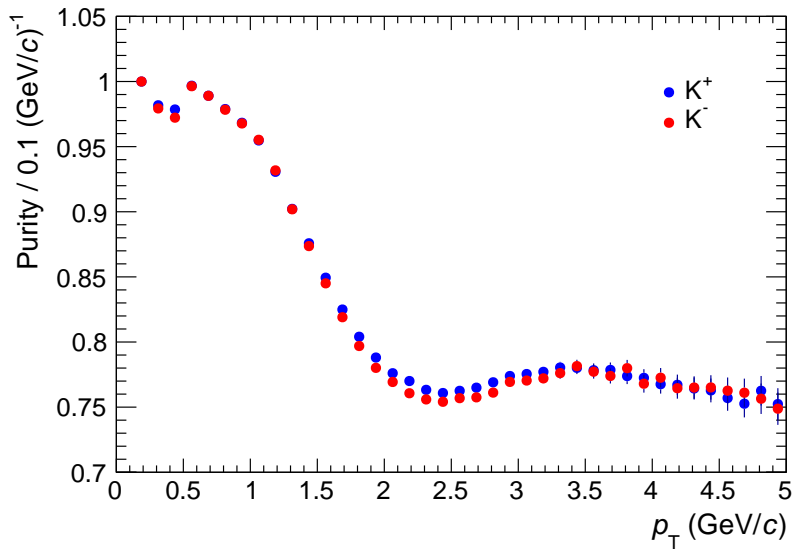


Figure 4.7: Purity of K^+ and K^- with sphericity cuts $0.7 < S_T < 1.0$

ϕ resonance

The ϕ s are obtained by combining the K^+ and K^- candidates, assuming their PDG masses. The resonance peak in the invariant mass distribution of the ϕ candidates is fitted with the voigt function, which is a convolution of a Gaussian (which accounts for the detector resolution) and a relativistic Breit-Wigner peak (which describes the ideal signal) [39]

$$\frac{dN}{dm_{K^+K^-}} = \frac{A\Gamma}{(2\pi)^{3/2}\sigma} \int_{-\infty}^{+\infty} \exp\left[-\frac{(m_{K^+K^-} - m')^2}{2\sigma^2}\right] \frac{1}{(m' - M_\phi)^2 + \Gamma^2/4} dm', \quad (4.6)$$

where A is a scaling factor, σ the Gaussian width, Γ the ϕ full width and M_ϕ the ϕ mass. The background is fitted with a quadratic polynomial.

Figure 4.8 shows the invariant mass distribution of K^+ and K^- with a sphericity of

$0.7 < S_T < 1.0$ for HM events, while Fig. 4.9 shows the same for MB events. In order to get as pure reconstructed ϕ s as possible, while still having enough candidates to conduct a femtoscopic analysis, a cut in the invariant mass spectra of $M_\phi \pm 8 \text{ MeV}/c$ is applied. A total of $5.30 \cdot 10^6$ ϕ s are reconstructed for high multiplicity data with an overall purity of 67.26 %, which means that the correlation signal has a non-negligible contribution arising from the combinatorial K^+K^- background. It is calculated the following

$$\text{Purity} = \frac{S}{S + B}, \quad (4.7)$$

where S corresponds to the integral over the signal and B is the corresponding background. There are in the order of magnitude of 10 less reconstructed ϕ s for MB events with only a yield of $7.35 \cdot 10^5$, even though the purity of 75.20% is slightly higher. For both HM and MB the mass from the fit M_ϕ is consistent with the PDG mass of $M_{\phi, \text{PDG}} = (1019.461 \pm 0.016) \text{ MeV}$ [38] within the detector resolution.

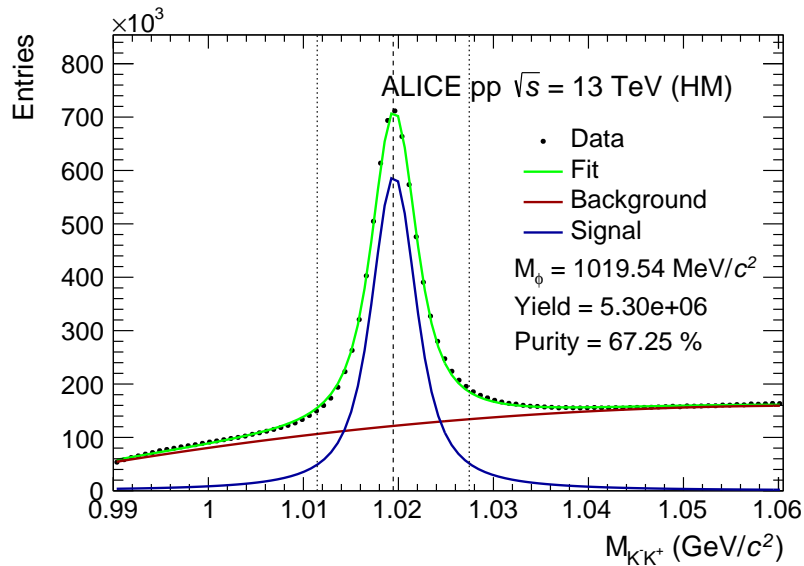


Figure 4.8: K^+K^- invariant mass distribution for high multiplicity events with sphericity cuts $0.7 < S_T < 1.0$. The dashed lines represent the $M_\phi \pm 8 \text{ MeV}/c$ selection for the femtoscopic analysis.

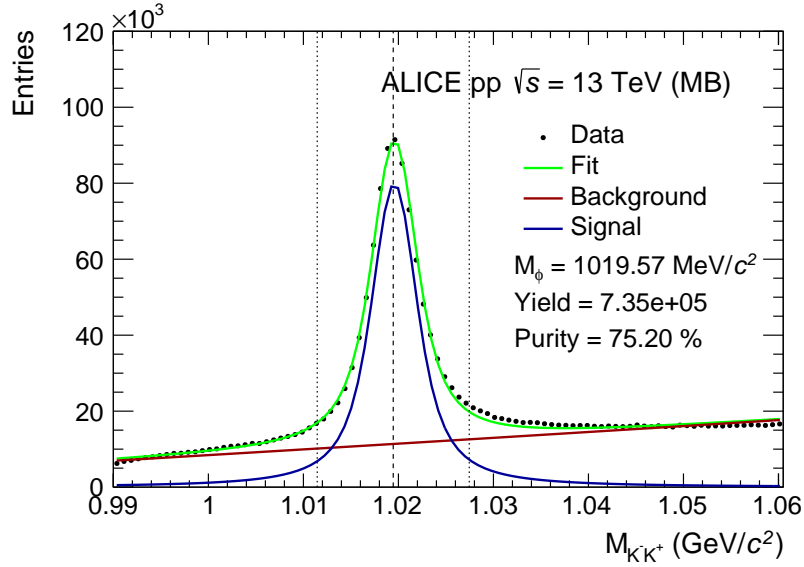
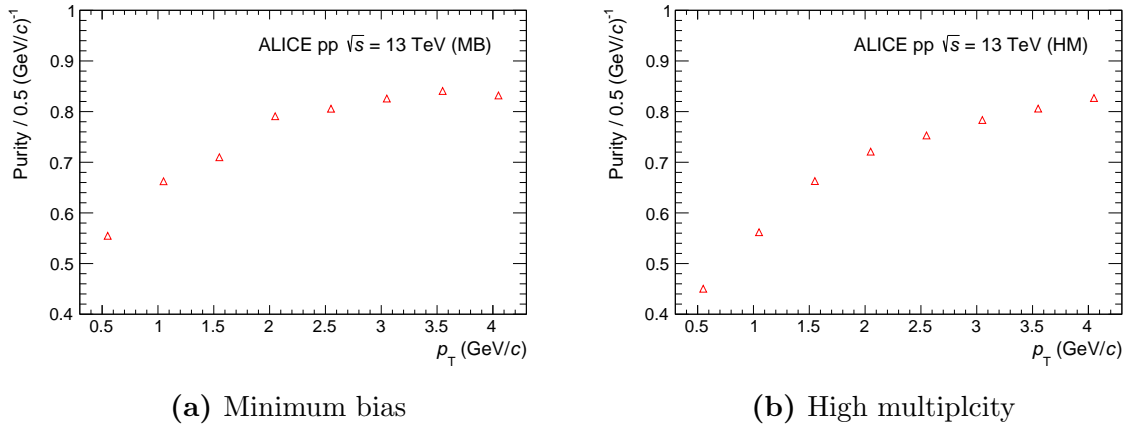


Figure 4.9: K^+K^- invariant mass distribution for minimum bias events with sphericity cuts $0.7 < S_T < 1.0$. The dashed lines represent the $M_\phi \pm 8 \text{ MeV}/c$ selection for the femtosopic analysis.

Figure 4.10 shows the ϕ purity as a function of the transverse momentum for MB and HM, which is computed in slices of $\Delta p_T = 0.5 \text{ GeV}/c$. For both HM and MB the purity is lower for small transverse momentum because of the larger combinatorial background.



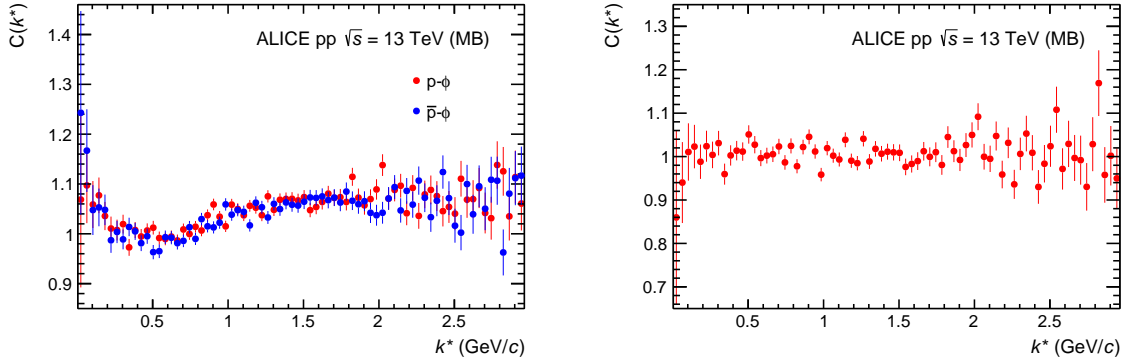
(a) Minimum bias

(b) High multiplicity

Figure 4.10: Purity of the reconstructed ϕ s as function of the transverse momentum for a sphericity of $0.7 < S_T < 1.0$

5 Correlation function

5.1 Minimum Bias



(a) The ϕ - p and ϕ - \bar{p} correlation function (b) Ratio between both correlation functions

Figure 5.1: Comparison of the ϕ - p and ϕ - \bar{p} correlation function for minimum bias events

Table 5.1: Minimum bias counts

total events without sphericity cuts	$1.6 \cdot 10^9$
total events $0.7 < S_T < 1.0$	$245 \cdot 10^6$
reconstructed ϕ yield	$7.35 \cdot 10^5$
Total ϕ - p pairs	$3.14 \cdot 10^5$
Total ϕ - \bar{p} pairs	$2.75 \cdot 10^5$
ϕ - p with $k^* < 200 \text{ MeV}/c$	2969
ϕ - \bar{p} with $k^* < 200 \text{ MeV}/c$	2605

To calculate the correlation function, minimum bias proton-proton events at $\sqrt{s} = 13 \text{ TeV}$ from 2016, 2017 and 2018 are used, the relevant event-, particle- and pair counts in the femtoscopic range are summarized in Table 5.1. The advantage of this data-set is the existence of Monte Carlo generated events, which can be used for the analysis. As there is no final state interaction, it is possible to determine the non-femtoscopic background by comparing MC data with experimental data.

In the following, data with sphericity event shape cuts of $0.7 < S_T < 1.0$ will be used. As the ϕ is its own antiparticle, first the correlation function of ϕ - p and ϕ - \bar{p} is calculated

separately. The corresponding pairs are formed using correlated particles from the same event and uncorrelated ones from different events by applying event mixing methods. The functions are normalized between 240 and 340 MeV/c and have a bin width of 40 MeV/c. Both correlation signals are shown in Fig. 5.1a and their ratio in Fig (5.1b). The latter is consistent with unity, which makes it possible to combine both ϕ -p and ϕ - \bar{p} pairs. This leads to a higher pair multiplicity and thus smaller statistical uncertainties in the correlation function.

Figure 5.2 shows the correlation signal from experimental p- ϕ \oplus \bar{p} - ϕ data – which is the combination of both pairs as mentioned before – and the one from generated events with no event shape cuts applied. One can clearly see the pattern of mini-jets between $k^* \sim 200$ MeV/c and $k^* \sim 1000$ MeV/c. Figure 5.3 shows both correlation functions with a sphericity cut of $0.7 < S_T < 1.0$ as comparison. The mini-jet background was significantly reduced due to strict cuts on the event shape. More important, one can see in both figures that the simulation describes the mini-jet background.

The minimum bias correlation function has still large uncertainties due to its small pair yield. Therefore, it is not reasonable to use this data set for further analyzing the ϕ -meson proton correlation function. High multiplicity is in the case of this analysis the better choice as the yield is significantly higher.

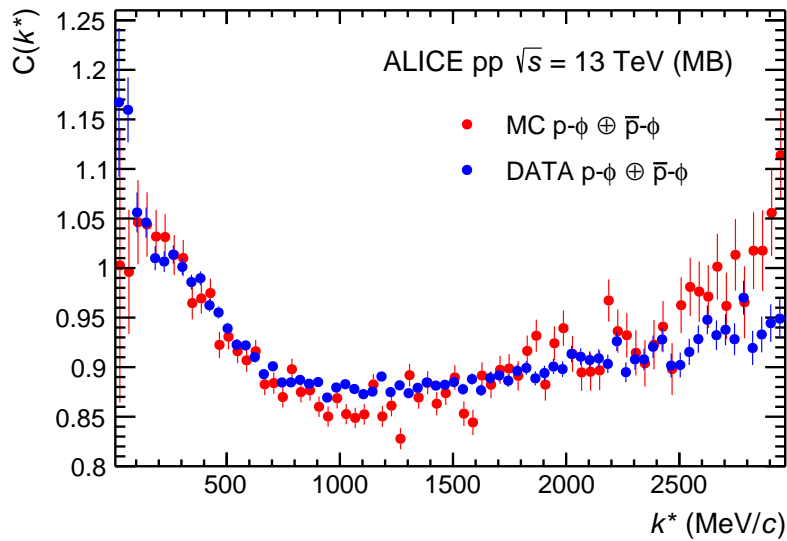


Figure 5.2: Correlation function of experimental data compared with MC generated events without any event shape cuts

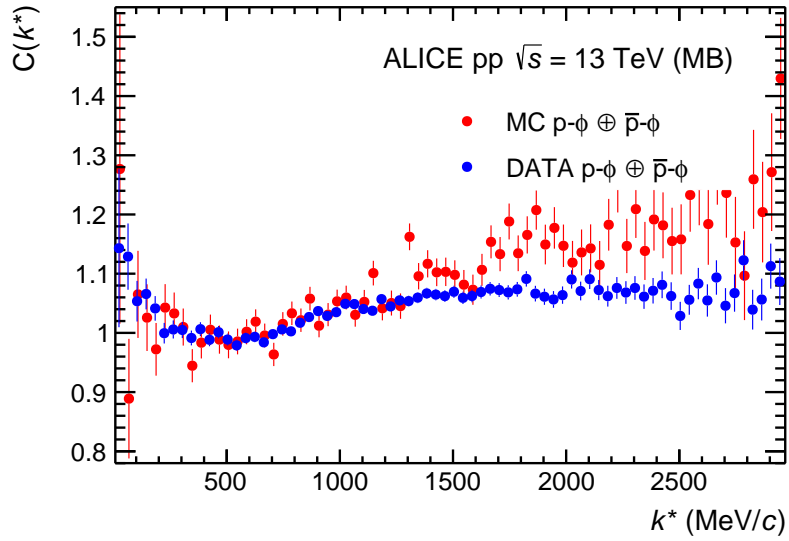
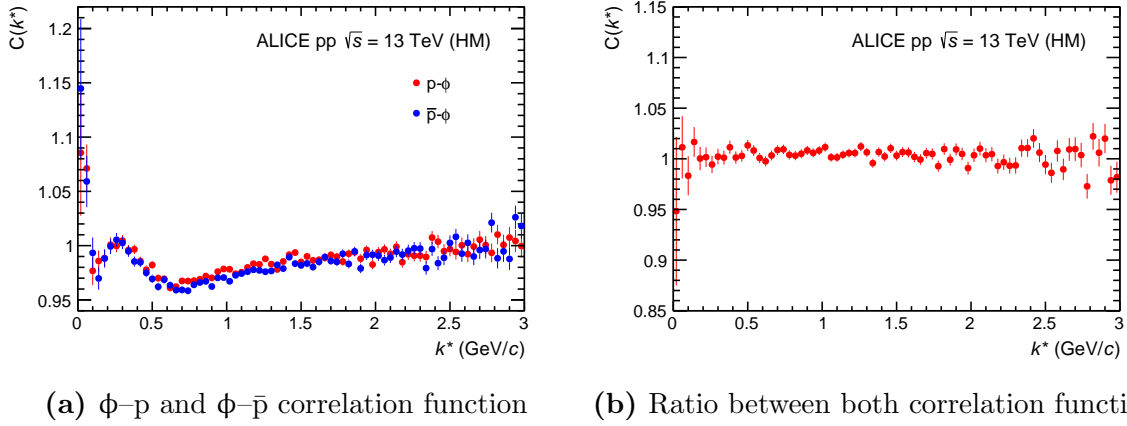


Figure 5.3: Correlation function for data and MC generated events with sphericity cuts $0.7 < S_T < 1.0$

5.2 High Multiplicity



(a) ϕ -p and ϕ - \bar{p} correlation function

(b) Ratio between both correlation functions

Figure 5.4: Comparison of the ϕ -p and ϕ - \bar{p} correlation function for high multiplicity events

In this section high multiplicity proton-proton events at $\sqrt{s} = 13$ TeV from 2016, 2017 and 2018 with sphericity cuts of $0.7 < S_T < 1.0$ are used to measure the ϕ -proton correlation function. All relevant yields and counts are summarized in Table 5.2. There are $3.48 \cdot 10^4$ ϕ -p pairs and $3.01 \cdot 10^4$ ϕ - \bar{p} pairs with $k^* < 200$ MeV/c available for the analysis, which is over 10 times more than for MB events in the relative momentum region relevant for the particle correlation. Both the ϕ -p and ϕ - \bar{p} correlation function

Table 5.2: High multiplicity counts

total events without sphericity cuts	$972 \cdot 10^6$
total events $0.7 < S_T < 1.0$	$541 \cdot 10^6$
reconstructed ϕ yield	$5.30 \cdot 10^6$
Total ϕ -p pairs	$4.63 \cdot 10^6$
Total ϕ - \bar{p} pairs	$4.03 \cdot 10^6$
ϕ -p with $k^* < 200 \text{ MeV}/c$	$3.55 \cdot 10^4$
ϕ - \bar{p} with $k^* < 200 \text{ MeV}/c$	$3.07 \cdot 10^4$

is shown in Fig. 5.4a and the ratio in Fig. 5.4b. Again, as the ratio is consistent with unity within the uncertainties, both can be combined to increase the pair multiplicity. Figure 5.5 shows the ϕ meson proton correlation function with and without sphericity cuts. Again the normalization range is $240 - 340 \text{ MeV}/c$ and the bin width is $40 \text{ MeV}/c$. Like for MB one can clearly see the signature of residual mini-jets as an enhancement between ~ 150 and $\sim 1000 \text{ MeV}/c$ peaking at $250 \text{ MeV}/c$ on the red graph, where no specific cuts were applied. A sphericity cut of $0.7 < S_T < 1.0$ (blue graph) leads to an effective suppression of the residual mini-jets background in the correlation signal. A small shoulder is still left between ~ 150 and $\sim 500 \text{ GeV}/c$, but the effect is only in the order of 5 %. The analysis is sensitive to the interaction between ϕ and proton, as there is a clear modulation of the signal in the range of the strong final state interaction $k^* < 200 \text{ MeV}$ and the interaction seems to be attractive.

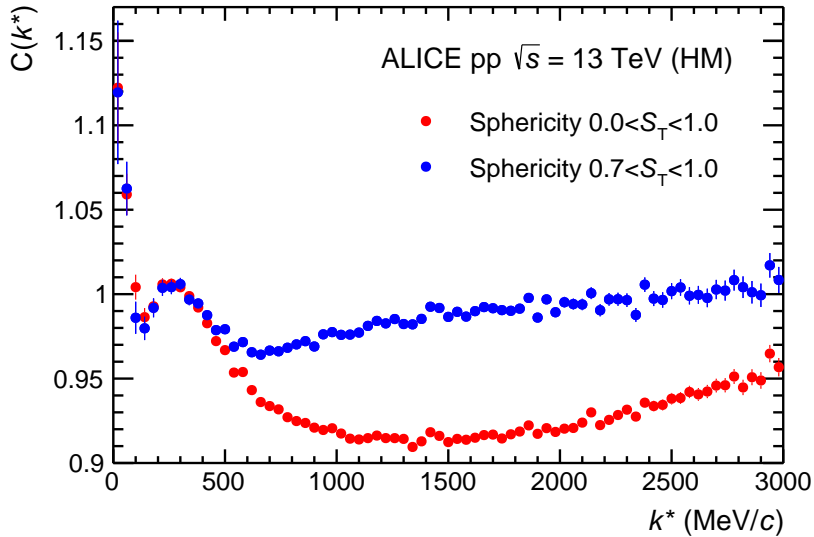


Figure 5.5: Correlation function with sphericity cuts (red graph) and without any event shape cuts (blue graph) for high multiplicity events

5.2.1 Sphericity vs. sphericity

In this part the difference between transverse sphericity and transverse sphericity will be shown in regard to their effect on the correlation function. Both are compared in Fig. 5.6. In order to have small statistical uncertainties while effectively suppressing the mini-jets a cut-range of $0.7 < S_T/S_0 < 1.0$ is used and one can see that sphericity cuts are slightly more efficient in reducing the background, as the enhancement is less high.

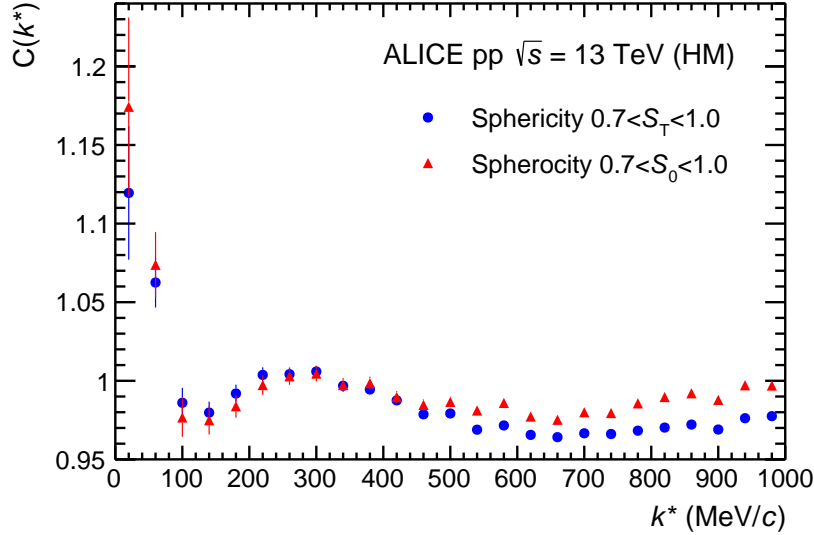


Figure 5.6: Correlation function with cuts on the event sphericity compared to the one with sphericity cuts for high multiplicity events

By moving the cut range to more spherical events, see Fig. 5.7, sphericity yields a better suppression of the mini-jets than sphericity but considerably reduces the amount of events. For $0.8 < S_0 < 1.0$ only $1.12 \cdot 10^8$ events are left for the analysis, which is only a third of the $0.7 < S_0 < 1.0$ event yield of $3.08 \cdot 10^6$. This results in larger uncertainties and makes sphericity cuts in general more useful for an analysis.

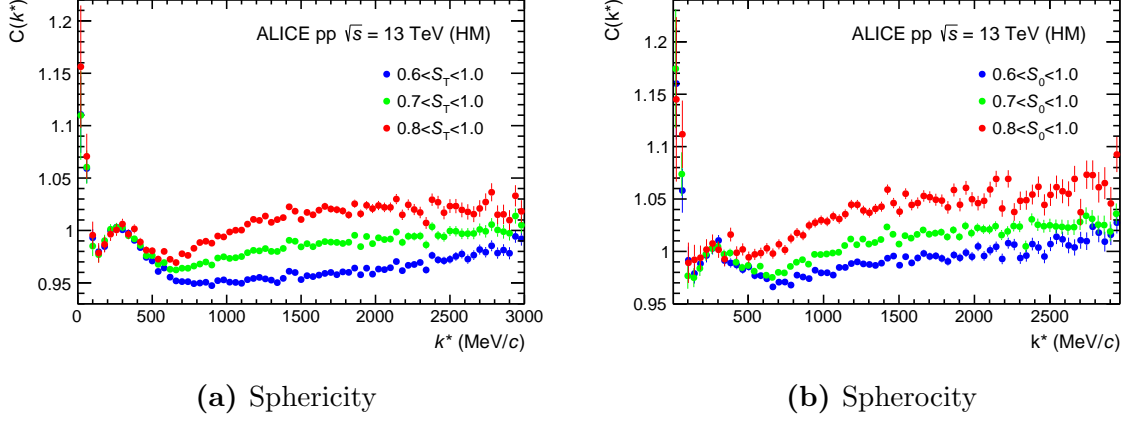


Figure 5.7: Correlation function with different ranges of event shape cuts for high multiplicity events

5.2.2 Background

Due to a ϕ purity of only 67.26 %, the combinatorial background of $p-(K^+K^-)$ has a non-negligible contribution to the measured correlation signal. Therefore, the sidebands, which correspond to intervals in the K^+K^- invariant mass distribution besides the ϕ resonance itself, have to be investigated in order to understand the mass-dependency and shape of the background correlation.

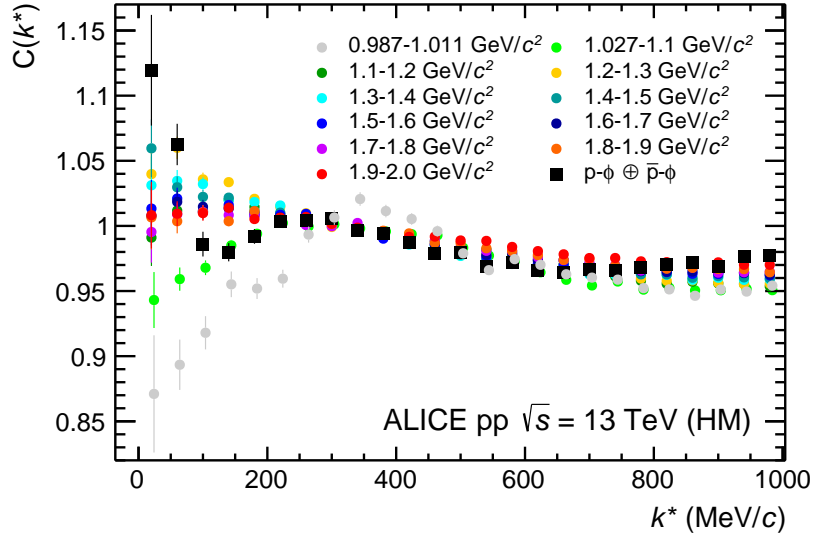


Figure 5.8: Correlation functions of $p-\phi \oplus \bar{p}-\phi$ and $p-(K^+K^-)$ for different intervals of $M_{K^+K^-}$

Figure 5.8 shows the correlation functions of different sidebands, covering a broad invariant mass spectrum from the $2 M_K = 2 \cdot 493.68 \text{ MeV} = 987.36 \text{ MeV}$ threshold to 2.0 GeV , compared with the actual $p\text{-}\phi \oplus \bar{p}\text{-}\phi$ signal. Their shape for $k^* > 200 \text{ MeV}$ is very similar and the left-over mini-jet background is present in every single correlation function with the same characteristic profile. But the shape of the correlation function in the femtoscopic region varies for the different intervals, as the invariant mass is related to the opening angle between the K^+ and K^- momentum, see Eq. 4.5. For low k^* , the angle is small and a two- or even three-body interaction due to Coulomb and strong interaction between the kaons and the proton is possible. For large angles and invariant mass there is no correlation possible as the particles are too far away from each other to experience a final state interaction, shown schematically in Fig. 5.9. This effect can be seen by looking at different sideband intervals: far enough away from the ϕ peak at large M_{K^\pm} , the correlation signal gets flat in the region of the strong interaction, which implies that the mini-jet background in the low k^* region could look similar.

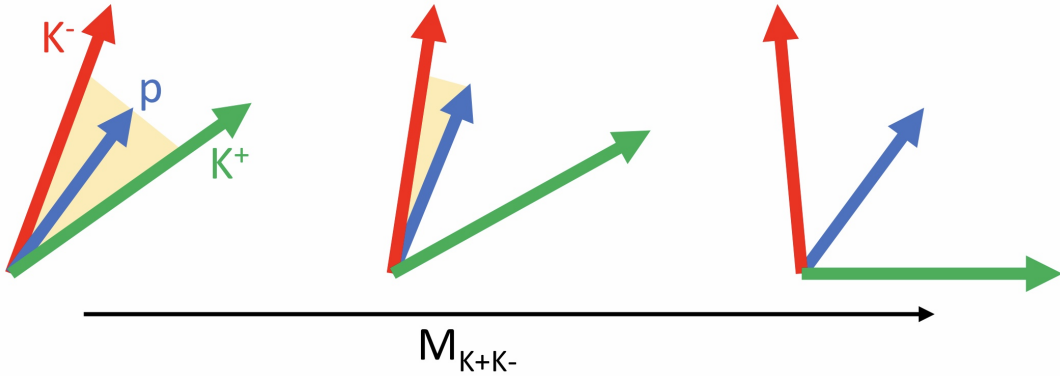


Figure 5.9: Schematic illustration of possible two- or even three-particle interactions between K^\pm and proton (yellow shaded)

The sidebands that are most relevant to determine the combinatorial background are the ones directly next to the ϕ peak, $0.987 < M_{K^+K^-} < 1.011 \text{ GeV}/c$ on the left and $1.027\text{--}1.1 \text{ GeV}/c$ on the right respectively, see Fig. 5.10. On both sides of the ϕ -peak the sideband correlation functions have a similar shape – the small difference is probably due to threshold effects and the lower pair yield of the sideband to the left of the peak – and one can assume that the $p\text{-}(K^+K^-)$ correlation signal originating from the background of the ϕ resonance in-between the sidebands resembles them. The sideband correlation deviates completely from the $p\text{-}\phi \oplus \bar{p}\text{-}\phi$ signal in the low k^* region. This corroborates that this femtoscopic analysis is sensitive to the actual final state interaction between ϕ -meson and proton.

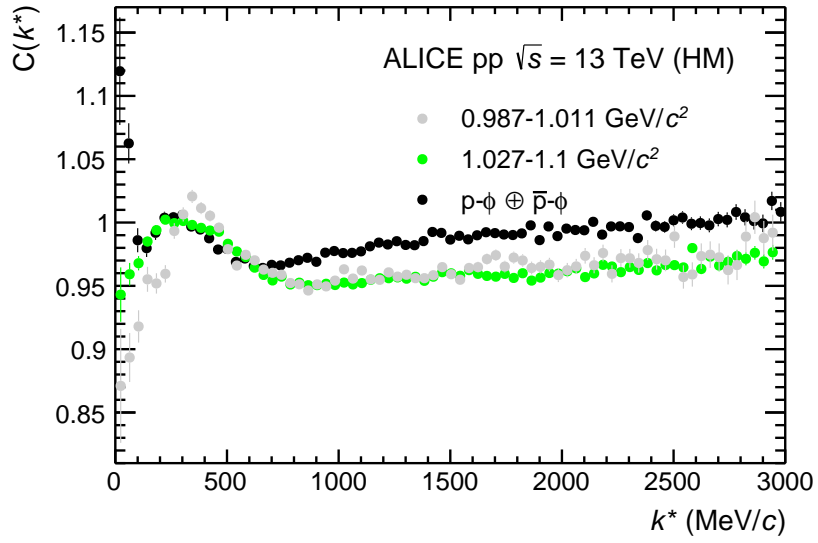


Figure 5.10: Correlation function of $p\text{-}\phi \oplus \bar{p}\text{-}\phi$ and $p\text{-}(K^+K^-)$ sidebands at low $M_{K^+K^-}$

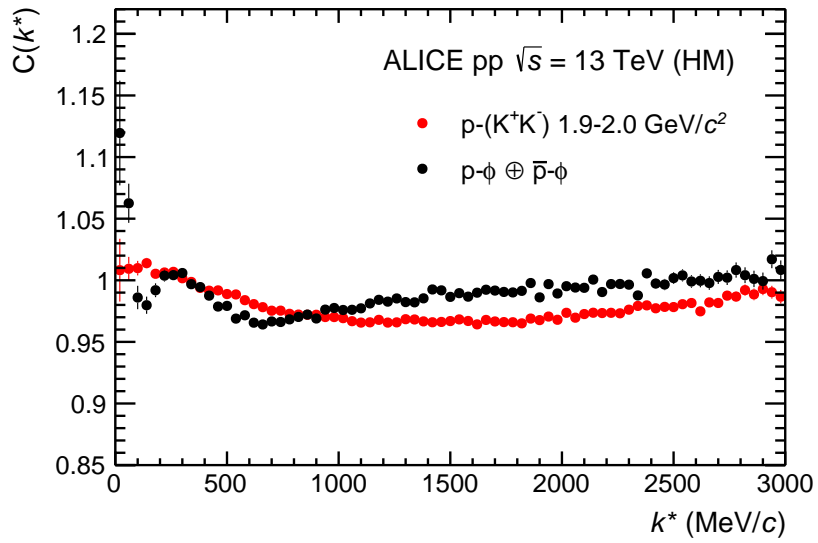


Figure 5.11: Correlation function of $p\text{-}\phi \oplus \bar{p}\text{-}\phi$ and sideband at invariant mass interval of $1.9 < M_{K^+K^-} < 2.0$ GeV/c

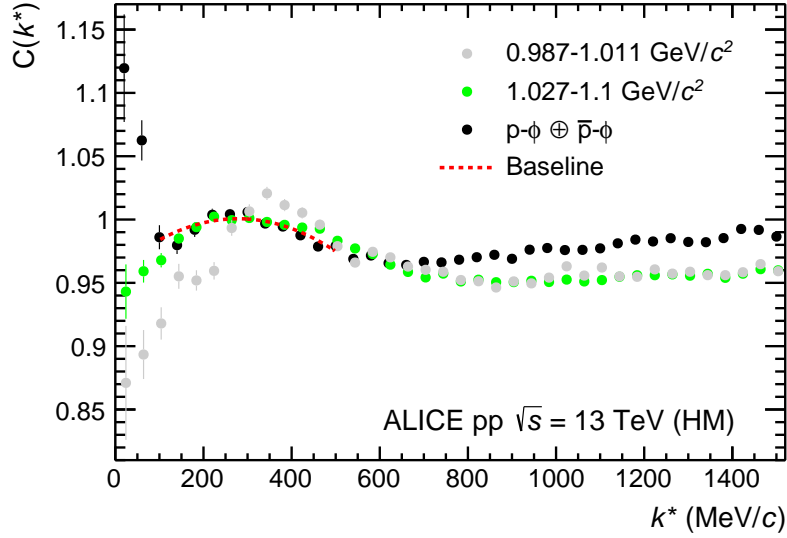


Figure 5.12: Quadratic baseline used for the CATS fit and correlation function of $p\text{-}\phi \oplus \bar{p}\text{-}\phi$ and $p\text{-}(K^+K^-)$ sidebands at low $M_{K^+K^-}$ as comparison

5.2.3 Fit with CATS

The correlation function is fitted with the Lednicky model using CATS (see Section 2.4) in order to determine the inverse scattering length f_0 and effective range d_0 of the interaction. Ideally the following fit function would be used

$$C_{fit}(k^*) = (a + b \cdot k^*) [1 + \lambda_{\phi-p} \cdot (C_{\phi-p}(k^*) - 1) + \lambda_{sideband} \cdot (C_{sideband}(k^*) - 1)]. \quad (5.1)$$

The λ parameters (Eq. 2.13) are obtained from the purity and fraction of primaries or secondaries from feed-down from a specific long-lived decay channel. For the ϕ -proton correlation they are $\lambda_{\phi-p} = 0.587$ and $\lambda_{sideband} = 0.327$. It is assumed that 100 % ϕ s are primary particles, as only a negligible amount are secondaries. The largest branching ratio is found to be of the D_S^+ decay, with $BR_{D_S^+ \rightarrow \phi \text{ anything}} = (15.7 \pm 1.0)\%$ [38], but as it contains the heavy \bar{s} and c quarks it is produced less abundantly.

As the non-femtoscopic mini-jet background has not been completely suppressed by event shape cuts, it is not possible to use a linear baseline. Therefore, as a first approach, the following fit is used

$$C_{fit}(k^*) = (a + b \cdot k^* + c \cdot k^{*2}) [1 + \lambda_{\phi-p} \cdot (C_{\phi-p}(k^*) - 1)] \quad (5.2)$$

Here a quadratic polynomial is used as baseline and is fitted within a range of 100 – 500 MeV/c. It accounts for the shape of the combinatorial $p\text{-}(K^+K^-)$ background including the remaining mini-jets, see Fig. 5.12. The exact shape of the non-femtoscopic mini-jet background in the low k^* area still has to be determined in the future using generated HM MC events for the analysis in order to improve the baseline of the fit. Also the $p\text{-}(K^+K^-)$ background in form of sideband correlations next to the ϕ -peak

suppressed by $\lambda_{sideband}$ has to be included subsequently. As source parameter a radius of 1.3 fm is assumed. The momentum smearing matrix is shown in Fig. 5.13 and corrects the fit function for detector effects on the momentum resolution by transforming the correlation function to the reconstructed momentum basis.

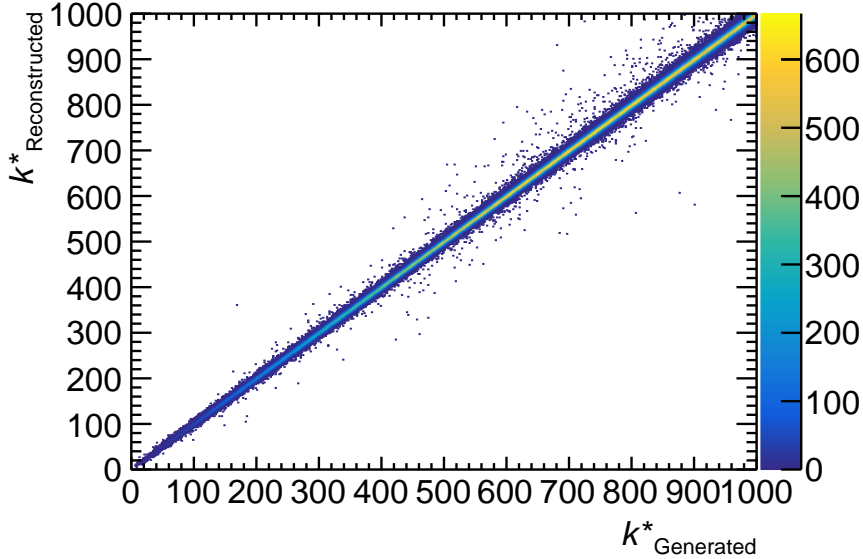


Figure 5.13: Momentum smearing matrix that compares the reconstructed relative momentum with the generated one from MC simulated data in MB

Figure 5.14 shows the correlation function with the final fit using the Lednický model in form of Eq. 5.2. The goodness of fit was determined by using a χ^2 test below 200 MeV/c, as this is the interesting region for the ϕ -proton final state interaction, with $\chi^2/\text{NDF} = 1.26$ as result. From this fit one gets an inverse scattering length of $1/f_0 = 1.9 \pm 0.7 \text{ fm}^{-1}$ and an effective range of $d_0 = 17 \pm 5 \text{ fm}$. This is the very first time the ϕ -p scattering parameters have been determined and it shows that the measurement is feasible. In order to probe if it is really the best fit or only a local χ^2 minimum, the parameters are varied between $0 \text{ fm} < d_0 < 20 \text{ fm}$ and $-5 \text{ fm}^{-1} < 1/f_0 < 5 \text{ fm}^{-1}$. For each combination the obtained fit function is compared to the data. The corresponding parameter phase space is shown in Fig. 5.15, where the contours visualize 1 σ , 2 σ , and 3 σ confidence level, respectively. This verifies that the fit from Fig. 5.2 is actually the best fit and in addition a huge area of the parameter phase space can be excluded. In particular, a repulsive ϕ -proton interaction can be excluded with more than 3 σ , which confirms the attractiveness of the ϕ -proton correlation.

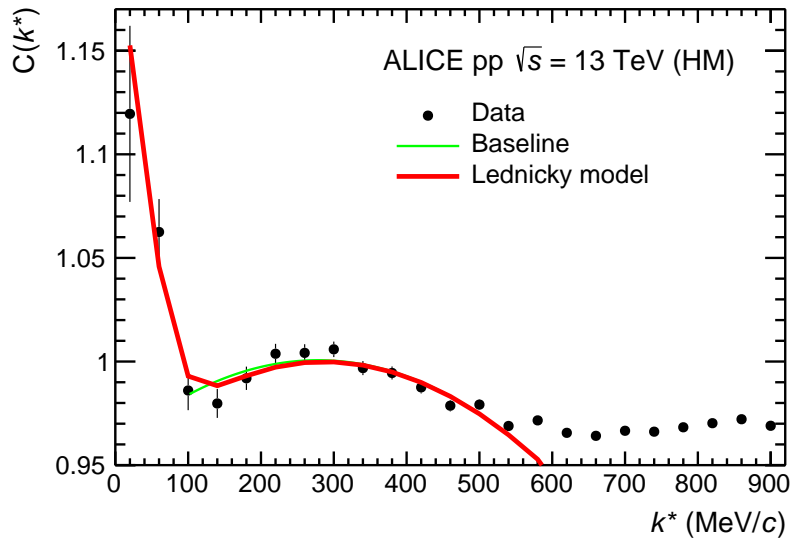


Figure 5.14: Correlation function fitted with the Lednicky model and a quadratic polynomial as baseline using CATS

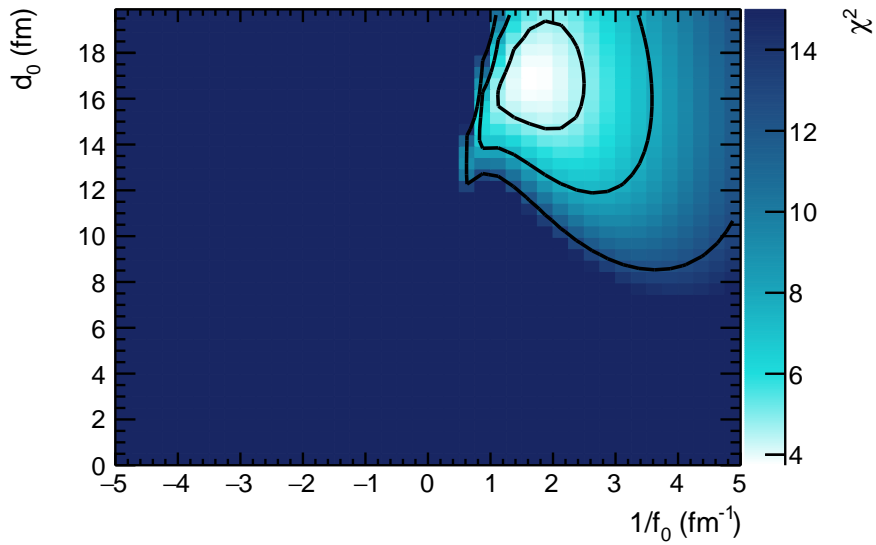


Figure 5.15: Degree of consistency of the correlation function modeled using the corresponding scattering parameters with the measured data. The contour lines correspond to 1, 2, and 3 σ confidence level.

6 Summary and Outlook

For the first time the ϕ -proton correlation function was studied and the scattering parameters determined by analyzing data from pp collisions at $\sqrt{s} = 13$ TeV measured with ALICE at the LHC during Run 2. Both minimum bias and high multiplicity triggered data from 2016, 2017 and 2018 was used.

The ϕ -mesons have been reconstructed using the method of invariant mass via their decay to K^+ and K^- , which has a branching ratio of $\text{BR}_{\phi \rightarrow K^+K^-} = (49.2 \pm 0.5)\%$. From high multiplicity events $5.30 \cdot 10^6$ ϕ candidates could be identified and from minimum bias $7.35 \cdot 10^5$, respectively.

To reduce the non-femtoscopic mini-jet background arising from low momentum transfer scatterings, which is also known from previous meson-baryon analyses, cuts on the event sphericity of $0.7 < S_T < 1.0$ have been applied. A total of $531 \cdot 10^6$ high multiplicity and $245 \cdot 10^6$ minimum bias events were available for the analysis. Also the event sphericity has been studied but no significant improvement in suppressing the mini-jets was obtained. As the purity of the reconstructed ϕ is about 70 %, also the combinatorial background of $p-(K^+K^-)$ had to be investigated as it contributes to the correlation signal.

The correlation function obtained from high multiplicity data has smaller uncertainties than the minimum bias one as more ϕ s were reconstructed and thus also more pairs were available for the analysis. Therefore, the high multiplicity correlation signal was fitted with the Lednicky model and a quadratic polynomial as baseline for the non-femtoscopic background in order to obtain the scattering parameters. The interaction between proton and ϕ is found to be attractive and the negative phase space of the scattering length could be excluded with more than 3σ . The best fit fields an inverse scattering length of $1/f_0 = 1.9 \pm 0.7 \text{ fm}^{-1}$ and an effective range of $d_0 = 17 \pm 5 \text{ fm}$.

This was a feasibility study as the description of the non-femtoscopic background needs to be improved and systematic errors have to be estimated. As next step the $p-K^+$, $p-K^-$ and $p-(K^+K^-)$ phase space has to be simulated using PHYTIA in order to understand the Coulomb and strong interaction between the two or three particles and its influence on the correlation function. In addition Monte Carlo generated high multiplicity events are needed to investigate how the remaining mini-jet background behaves in the low k^* region, which is sensitive to the final state interaction. Both are essential in order to improve the fit of the correlation function and understand the additional physical processes that contribute besides the final state interaction between ϕ and proton itself.

Bibliography

- [1] A. Maire. Phase diagram of QCD matter : Quark-Gluon Plasma. General Photo, Jun 2015. URL: <https://cds.cern.ch/record/2025215>.
- [2] J. M. Lattimer and M. Parakash. The Physics of Neutron Stars. *Science, New Series*, 302:536–542, 2004. URL: <https://doi.org/10.1126/science.1090720>.
- [3] F. Özel and P. Freire. Masses, Radii, and the Equation of State of Neutron Stars. *Annual Review of Astronomy and Astrophysics*, 54(1):401–440, 2016. URL: <https://doi.org/10.1146/annurev-astro-081915-023322>.
- [4] G. Baym, T. Hatsuda, T. Kojo, P. D. Powell, Y. Song, and T. Takatsuka. From hadrons to quarks in neutron stars: a review. *Reports on Progress in Physics*, 81(5):056902, mar 2018. URL: <https://doi.org/10.1088/1361-6633/aaae14>, doi:10.1088/1361-6633/aaae14.
- [5] J. Thierry and L. Courvoisier. *High Energy Astrophysics: An Introduction*. Springer, 2013.
- [6] R. C. Tolman. Static Solutions of Einstein’s Field Equations for Spheres of Fluid. *Phys. Rev.*, 55:364–373, Feb 1939. URL: <https://link.aps.org/doi/10.1103/PhysRev.55.364>.
- [7] J. R. Oppenheimer and G. M. Volkoff. On Massive Neutron Cores. *Phys. Rev.*, 55:374–381, Feb 1939. URL: <https://link.aps.org/doi/10.1103/PhysRev.55.374>.
- [8] J. Antoniadis and et al. A Massive Pulsar in a Compact Relativistic Binary. *Science*, 340(6131), Apr 2013. URL: <https://doi.org/10.1126/science.1233232>.
- [9] S. Acharya et al. p-p, p- Λ and Λ - Λ correlations studied via femtoscopy in pp reactions at $\sqrt{s} = 7$ TeV. *Phys. Rev.*, C99(2):024001, 2019. arXiv:1805.12455, doi:10.1103/PhysRevC.99.024001.
- [10] J. Haidenbauer, U. G. Meißner, N. Kaiser, and W. Weise. Lambda-nuclear interactions and hyperon puzzle in neutron stars. *Eur. Phys. J.*, A53(6):121, 2017. arXiv:1612.03758, doi:10.1140/epja/i2017-12316-4.
- [11] S. Weissenborn, D. Chatterjee, and J. Schaffner-Bielich. Hyperons and massive neutron stars: The role of hyperon potentials. *Nuclear Physics A*, 881:62 – 77, 2012. Progress in Strangeness Nuclear Physics. URL: <https://doi.org/10.1016/j.nuclphysa.2012.02.012>.

- [12] T. Inoue. Strange Nuclear Physics from QCD on Lattice. *AIP Conf. Proc.*, 2130(1):020002, 2019. URL: <https://aip.scitation.org/doi/abs/10.1063/1.5118370>, arXiv:1809.08932, doi:10.1063/1.5118370.
- [13] S. Acharya et al. First observation of an attractive interaction between a proton and a multi-strange baryon. *Submitted to: Phys. Rev. Lett.*, 2019. URL: <https://arxiv.org/abs/1904.12198>, arXiv:1904.12198.
- [14] S. Acharya et al. Scattering studies with low-energy kaon-proton femtoscopy in proton-proton collisions at the LHC. *arXiv e-prints*, 2019. arXiv:1905.13470.
- [15] M. A. Lisa, S. Pratt, R. Soltz, and U. Wiedemann. FEMTOSCOPY IN RELATIVISTIC HEAVY ION COLLISIONS: Two Decades of Progress. *Annual Review of Nuclear and Particle Science*, 55(1):357–402, 2005. URL: <https://doi.org/10.1146/annurev.nucl.55.090704.151533>, doi:10.1146/annurev.nucl.55.090704.151533.
- [16] S. Pratt. Pion Interferometry for Exploding Sources. *Phys. Rev. Lett.*, 53:1219–1221, Sep 1984. URL: <https://link.aps.org/doi/10.1103/PhysRevLett.53.1219>, doi:10.1103/PhysRevLett.53.1219.
- [17] U. Heinz and B. V. Jacak. Two-Particle Correlations in Relativistic Heavy-Ion Collisions. *Annual Review of Nuclear and Particle Science*, 49(1):529–579, 1999. URL: <https://doi.org/10.1146/annurev.nucl.49.1.529>.
- [18] G. Kopylov. Like particle correlations as a tool to study the multiple production mechanism. *Physics Letters B*, 50(4):472 – 474, 1974. URL: <http://www.sciencedirect.com/science/article/pii/0370269374902639>, doi:[https://doi.org/10.1016/0370-2693\(74\)90263-9](https://doi.org/10.1016/0370-2693(74)90263-9).
- [19] R. Lednicky. Finite-size effects on two-particle production in continuous and discrete spectrum. *Phys. Part. Nucl.*, 40:307–352, 2009. arXiv:nucl-th/0501065, doi:10.1134/S1063779609030034.
- [20] R. Lednicky and V. L. Lyuboshits. Final State Interaction Effect on Pairing Correlations Between Particles with Small Relative Momenta. *Sov. J. Nucl. Phys.*, 35:770, 1982. [*Yad. Fiz.*35,1316(1981)].
- [21] D. L. Mihaylov, V. Mantovani Sarti, O. W. Arnold, L. Fabbietti, B. Hohlweger, and A. M. Mathis. A femtoscopic correlation analysis tool using the Schrödinger equation (CATS). *The European Physical Journal C*, 78(5):394, May 2018. URL: <https://doi.org/10.1140/epjc/s10052-018-5859-0>, doi:10.1140/epjc/s10052-018-5859-0.
- [22] J.-L. Caron. CERN Accelerator Complex (operating and approved projets).. Chaîne des accélérateurs du CERN (en fonctionnement et avec les projets approuvés)., Jun 1991. AC Collection. Legacy of AC. Pictures from 1992 to 2002. URL: <https://cds.cern.ch/record/841493>.

- [23] L. Evans and P. Bryant. LHC Machine. *JINST*, 3:S08001, 2008. doi:10.1088/1748-0221/3/08/S08001.
- [24] J. Alme and et al. The ALICE TPC, a large 3-dimensional tracking device with fast readout for ultra-high multiplicity events. *Nuclear Instruments and Methods in Physics Research Section A: Accelerators, Spectrometers, Detectors and Associated Equipment*, 622(1):316 – 367, 2010. URL: <http://www.sciencedirect.com/science/article/pii/S0168900210008910>, doi:<https://doi.org/10.1016/j.nima.2010.04.042>.
- [25] B. B. Abelev et al. Performance of the ALICE Experiment at the CERN LHC. *Int. J. Mod. Phys.*, A29:1430044, 2014. arXiv:1402.4476, doi:10.1142/S0217751X14300440.
- [26] K. Aamodt et al. The ALICE experiment at the CERN LHC. *JINST*, 3:S08002, 2008. doi:10.1088/1748-0221/3/08/S08002.
- [27] The ALICE Time Projection Chamber (TPC) [online]. 2008. URL: http://aliceinfo.cern.ch/Public/en/Chapter2/Chap2_TPC.html [last checked 2019-08-31].
- [28] B. Povh, K. Rith, C. Scholz, and F. Zetsche. *Teilchen und Kerne: Eine Einführung in die physikalischen Konzepte; 8th ed.* Springer-Lehrbuch. Springer, Heidelberg, 2009. Also available in English version. URL: <https://cds.cern.ch/record/1494496>.
- [29] A. P. Kalweit. ALICE TPC dE/dx performace in Run2 13 TeV (0.2T), 2015. Accessed on 2019-08-21. URL: <https://alice-figure.web.cern.ch/node/8670>.
- [30] T. Jimenez. TOF beta vs momentum performance in pp at 13 TeV (LHC15f), 2016. Accessed on 2019-08-21. URL: <https://alice-figure.web.cern.ch/node/9564>.
- [31] The Worldwide LHC Computing Grid. Accessed on 2019-08-11. URL: <https://home.cern/science/computing/worldwide-lhc-computing-grid>.
- [32] R. Derradi De Souza. V0M/ \langle V0M \rangle distributions MB VHM triggers, 2017. Accessed on 2019-08-21. URL: <https://alice-figure.web.cern.ch/node/11516>.
- [33] L. Bianchi. Particle-to-pion ratio as a function of multiplicity in pp7, pp13, p-Pb5, p-Pb8, Pb-Pb5 and Xe-Xe, 2019. Accessed on 2019-08-21. URL: <https://alice-figure.web.cern.ch/node/15504>.
- [34] The ALICE Collaboration. Multiplicity dependence of jet-like two-particle correlation structures in p–Pb collisions at $\sqrt{s_{NN}} = 5.02$ TeV. *Physics Letters B*, 741:38 – 50, 2015. URL: <http://www.sciencedirect.com/science/article/pii/S0370269314008302>, doi:<https://doi.org/10.1016/j.physletb.2014.11.028>.

- [35] A. Ortiz. Transverse sphericity of charged particles in minimum bias p-p collision in ALICE at the LHC. In *Proceedings, Physics at LHC 2011: International Conference held in Perugia, Italy, June 6-11, 2011*, 2011. URL: <http://www.slac.stanford.edu/econf/C1106061/proceedpdf/091-094.pdf>, arXiv:1110.2278.
- [36] The ALICE Collaboration. Transverse sphericity of primary charged particles in minimum bias proton-proton collisions at $\sqrt{s} = 0.9, 2.76$ and 7 TeV. *The European Physical Journal C*, 72(9):2124, Sep 2012. URL: <https://doi.org/10.1140/epjc/s10052-012-2124-9>, doi:10.1140/epjc/s10052-012-2124-9.
- [37] A. Banfi, G. P. Salam, and G. Zanderighi. Phenomenology of event shapes at hadron colliders. *Journal of High Energy Physics*, 2010(6):38, Jun 2010. URL: [https://doi.org/10.1007/JHEP06\(2010\)038](https://doi.org/10.1007/JHEP06(2010)038), doi:10.1007/JHEP06(2010)038.
- [38] Review of Particle Physics. *Phys. Rev. D*, 98:030001, Aug 2018. URL: <https://link.aps.org/doi/10.1103/PhysRevD.98.030001>, doi:10.1103/PhysRevD.98.030001.
- [39] A. G. Knospe et al. Measurement of phi Mesons at Mid-Rapidity in Minimum-Bias pp Collisions at 13 TeV. 2017. URL: <https://alice-notes.web.cern.ch/node/466>.